JOURNAL OF GEOPHYSICAL RESEARCH, VOL. 114, B11305, doi:10.1029/2009JB006529, 2009

Self-similar slip pulses during rate-and-state earthquake nucleation

Allan M. Rubin[1] and Jean-Paul Ampuero[2]

Received 9 April 2009; revised 6 July 2009; accepted 22 July 2009; published 5 November 2009.

[1] For a wide range of conditions, earthquake nucleation zones on rate- and state-dependent faults that obey either of the popular state evolution laws expand as they accelerate. Under the "slip" evolution law, which experiments show to be the more relevant law for nucleation, this expansion takes the form of a unidirectional slip pulse. In numerical simulations these pulses often tend to approach, with varying degrees of robustness, one of a few styles of self-similar behavior. Here we obtain an approximate self-similar solution that accurately describes slip pulses growing into regions initially sliding at steady state. In this solution the length scale over which slip speeds are significant continually decreases, being inversely proportional to the logarithm of the maximum slip speed V_{max}, while the total slip remains constant. This slip is close to $D_c(1-a/b)^{-1}$, where D_c is the characteristic slip scale for state evolution and a and b are the parameters that determine the sensitivity of the frictional strength to changes in slip rate and state. The pulse has a "distance to instability" as well as a "time to instability," with the remaining propagation distance being proportional to $(1-a/b)^{-2}$ $[\ln(V_{max}\theta_{bg}/D_c)]^{-1}$, where θ_{bg} is the background state into which the pulse propagates. This solution provides a reasonable estimate of the total slip for pulses growing into regions that depart modestly from steady state.

Citation: Rubin, A. M., and J.-P. Ampuero (2009), Self-similar slip pulses during rate-and-state earthquake nucleation, *J. Geophys. Res.*, *114*, B11305, doi:10.1029/2009JB006529.

1. Introduction

[2] One motivation for developing constitutive laws for fault slip has been to model quasi-static earthquake nucleation. An early goal of such models was to assess the feasibility of detecting the nucleation phase of large earthquakes, hopefully with enough lead time to be useful for hazards mitigation [*Dieterich and Kilgore*, 1996]. It is also conceivable that the nucleation process sets the stage for the earliest portions of dynamic rupture [*Ellsworth and Beroza*, 1995], seismic signals from which might be used for earthquake early warning systems [*Olson and Allen*, 2005]. More recently, the same models that have been applied to nucleation have been used to study episodic slow slip in subduction zones [*Kato*, 2003; *Shibazaki and Iio*, 2003; *Liu and Rice*, 2005; *Rubin*, 2008]. In addition, a professed goal of ongoing experiments along the San Andreas fault and in deep South African mines is to detect the nucleation of small earthquakes at seismogenic depths [*Ellsworth et al.*, 2007; *Reches et al.*, 2004]. Interpreting such observations is likely to require a greater understanding of nucleation than we currently possess.

[3] Impediments to using numerical models to understand earthquake nucleation come from at least three sources: (1) uncertainty regarding the appropriate constitutive law for friction, (2) uncertainty regarding the relevant initial and boundary conditions along the fault, and (3) the difficulty in discerning how the friction law interacts with elasticity to define the characteristics of the nucleation zone. Uncertainty regarding the appropriate values of the frictional parameters is also an issue, but this probably pales in comparison to item 1. It is the nonlinearity of the governing equations that makes items 2 and 3 such significant hurdles. The complexity of elastic/frictional systems, and their sensitivity to both material properties and loading conditions, can make it difficult to extrapolate beyond the results of numerical simulations already carried out.

[4] For modeling quasi-static fault slip, rate- and state-dependent friction is thought to be a good compromise between simplicity and completeness [*Dieterich*, 1979; *Ruina*, 1983; *Rice et al.*, 2001]. *Rubin and Ampuero* [2005] obtained analytical estimates of the length and time scales of nucleation (addressing item 3 above) for the particular case of faults obeying the "aging" law for state evolution. For laboratory values of the rate-and-state parameters a and b and a seemingly wide range of initial and boundary conditions (e.g., relatively homogeneous faults under steady loading), such nucleation zones grow as quasi-statically expanding cracks and can approach a well-defined limiting size. This size is much larger than both that observed numerically by *Dieterich* [1992], and

[1]Department of Geosciences, Princeton University, Princeton, New Jersey, USA.
[2]Seismological Laboratory, California Institute of Technology, Pasadena, California, USA.

0148-0227/09/2009JB006529$09.00

that anticipated on the basis of critical stiffness arguments [*Rice et al.*, 2001]. Subsequent work has shown that this nucleation length arises also in radiation damping or fully elastodynamic earthquake cycle simulations that include adjoining velocity-weakening and velocity-strengthening regions (e.g., *Rubin* [2008, Figure 6] and *Chen and Lapusta* [2009, Figure 6], noting in the latter case that the length scale in 3-D is larger than in 2-D by the factor $\pi^2/4$).

[5] This crack-like expansion and large size result from the large increase in fracture energy with increasing slip speed implied by the aging law. This large increase in fracture energy in turn comes from the increase in the effective slip-weakening distance with the logarithm of the velocity jump at the margins of the expanding nucleation zone. However, as was noted in retrospect by *Rubin and Ampuero* [2005], there is no experimental evidence for this increase in slip-weakening distance. Experiments show instead that the slip-weakening distance seems to be independent of the magnitude of the velocity jump [*Nakatani*, 2001], a property that is well modeled by the "slip" evolution law [*Ruina*, 1983; *Bayart et al.*, 2006].

[6] *Ampuero and Rubin* [2008] found that for the slip law, nucleation zones expand not as cracks but as unidirectional slip pulses. Although they noted that their simulations appeared nearly self-similar in many respects, they were unable to obtain analytical descriptions comparable to those for the aging law. In this paper we derive an approximate self-similar solution for a particular class, and arguably the most basic class, of these slip pulses. By self-similar we mean that given a solution for any particular quantity (e.g., slip) as a function of position at one time, one can determine that same quantity at any later time simply by a suitable rescaling of the relevant coordinate axes. Such solutions, and even the scaling relations alone, can be very useful for interpreting complex numerical simulations and extrapolating beyond those already carried out. Scaling of the position axis is done here in the reference frame of the moving pulse tip. Determining the time dependence of the solution explicitly requires solving a transcendental equation for the maximum slip speed; however, that time dependence can be expressed much more simply in terms of the maximum slip speed itself, so we emphasize that view here. Some pulse attributes, such as the scaling of the total slip and stress drop with a/b, can be deduced from a general consideration of the observed self-similarity alone; this is the subject of section 4. Section 5 outlines the particular self-similar solution, which is needed to estimate the detailed spatial variation of slip and the rate of acceleration to instability. We also compare the scaling of nucleation under the slip and aging laws, and, in light of items 1 and 2 enumerated above, consider when the pulses described here might be relevant to natural faults.

2. Background

[7] We adopt a standard equation for the frictional strength τ,

$$\tau = \sigma\left[f^* + a\ln\frac{V}{V^*} + b\ln\frac{V^*\theta}{D_c}\right] \tag{1}$$

[e.g., *Marone*, 1998], where σ is the effective normal stress, V is the sliding velocity, θ is the variable with units of time describing the fault state, D_c is the characteristic sliding distance for the evolution of θ, and a and b determine the response to changes in sliding velocity and state (for a listing of frequently cited parameters see Table 1). f^* and V^* are reference values of the friction and velocity and exert no influence on the system. Characteristic laboratory values of D_c are $1-100$ μm, while a and b are typically of order 10^{-2}. When $a < b$ the fault is steady state velocity weakening and instability is possible; we assume this to be the case here. Laboratory values of a/b are very often >0.9, i.e., close to velocity neutral, even for velocity-weakening faults [*Kilgore et al.*, 1993; *Blanpied et al.*, 1998].

[8] For quasi-static deformations we equate the frictional strength from (1) with the fault stress, which we partition into a boundary condition $\tau^{\infty}(x, t)$ and an elastic component $\tau^{el}(x, t)$ due to nonuniform fault slip. In two dimensions the static elastic stresses due to nonuniform slip are

$$\tau^{el}(x) = \frac{\mu'}{2\pi}\int_{-\infty}^{\infty}\frac{d\delta/ds}{s-x}ds, \tag{2}$$

where δ is slip and μ' is the elastic shear modulus for antiplane deformation or the shear modulus divided by one minus Poisson's ratio for plane strain deformation.

[9] To close the system of equations we need an evolution law for the state variable. Two have been commonly used, both largely empirical:

$$\dot{\theta} = 1 - \frac{V\theta}{D_c} \qquad \text{(Aging law)}; \tag{3}$$

$$\dot{\theta} = -\frac{V\theta}{D_c}\ln\frac{V\theta}{D_c} \qquad \text{(Slip law)}. \tag{4}$$

Both laws exhibit steady state behavior ($\dot{\theta} = 0$) when $V\theta/D_c = 1$, and for $V\theta/D_c \sim 1$ they are asymptotically identical. When $V\theta/D_c \ll 1$, $\dot{\theta} \sim 1$ for the aging law (time-dependent strengthening) but $\dot{\theta} \ll 1$ for the slip law (no evolution in the absence of slip). The former behavior is more consistent with the observed strengthening during the "hold" portions of slide-hold-slide experiments, when slip speeds are extremely low and $V\theta/D_c \ll 1$ [*Dieterich and Kilgore*, 1994; *Beeler et al.*, 1994]. However, it is the behavior of the fault from $V\theta/D_c \sim 1$ to $V\theta/D_c \gg 1$ that determines the nucleation style [*Rubin and Ampuero*, 2005; *Ampuero and Rubin*, 2008; *Rubin*, 2008, Figure A1]. The pertinent difference between the laws for $V\theta/D_c \gg 1$ is that the effective slip-weakening distance for the return to steady state increases as $\log(V\theta/D_c)$ for the aging law, but is independent of $V\theta/D_c$ for the slip law. Laboratory experiments are much more consistent with the slip law in this regard, and in fact that law appears to work quite well when $V\theta/D_c \gg 1$ [*Ruina*, 1983; *Bayart et al.*, 2006], at least at slip speeds up to hundreds of microns per second. This is the motivation for obtaining an analytic description of nucleation under the slip law.

[10] As discussed by *Rubin and Ampuero* [2005] and *Ampuero and Rubin* [2008], the velocity jump at the margin of an expanding nucleation zone is close enough to instantaneous that it can be treated as such when estimating the

Table 1. Notation

Parameter	Description
a; b	Coefficients of the rate-and-state direct and evolution effects (equation (1))
C	Acceleration coefficient (equations (19) and (B4))
C_{age}	Acceleration coefficient in the crack expansion regime of aging law nucleation (equation (27))
D	Total slip within pulse (analytical approximation)
D_c	Characteristic slip distance in the evolution law
f, f'	Slip function and its spatial derivative (equation (17))
g, g'	Stress drop function and its derivative (equation (20))
$g_{\min}$	g at the stress minimum behind the pulse front
G	Mechanical energy release rate (equation (9))
G_c	Fracture energy (equation (5))
K_c	Fracture toughness (equation (7))
l	Location of pulse front
L	Characteristic nucleation length scale
L_b	Relevant length scale for $V\theta/D_c \gg 1$ (equation (8))
p	Slip growth exponent (equation (11))
R	Length of the slip-weakening region behind the pulse front (equation (16))
t^*	Time of instability
V	Slip speed
V_{bg}	Background slip speed prior to the approach of the pulse front
$V_{\max}$	Maximum slip speed behind the pulse front
V_{prop}	Propagation speed of the pulse front
w	Pulse half-width
W	Scaled normalized pulse half-width $(w/L_b)\Psi_0$ (equation (40))
x'	Distance behind the pulse front
X	Scaled normalized distance behind the pulse front $(x'/L_b)\Psi_0$ (equation (17))
X_{Vm}; f'_{Vm}	X and f' evaluated at the location of $V_{\max}$
δ	Slip distance
δ_c	Effective slip-weakening distance at the pulse front
θ	State variable
θ_{bg}	Value of θ prior to the arrival of the pulse front
μ'	μ (antiplane strain) or $\mu/(1-\nu)$ (plane strain), where μ is shear modulus and ν is Poisson's ratio
σ	Effective normal stress
τ	Shear stress
$\Delta\tau$	Stress drop
$\Delta\tau_{\min}$	$\Delta\tau$ at the stress minimum behind the pulse front
$\Delta\tau_{p-r}$	Peak-to-minimum strength drop at the pulse front
$\Delta\overline{\tau}$	Average stress drop within the pulse (analytical approximation)
$\nabla\tau$	Stress gradient within the pulse (analytical approximation)
Ψ_0	$\ln(V_{\max}\theta_{bg}/D_c)$; determines the fracture energy
Ψ_{bg}	$\ln(V_{bg}\theta_{bg}/D_c)$

stress evolution behind the front. With this approximation, the fracture energy G_c for the slip law is

$$G_c = b\sigma D_c \ln\frac{V_{\max}\theta_{bg}}{D_c}, \tag{5}$$

where $V_{\max}$ is the maximum slip speed behind the nucleation front and θ_{bg} is the background value of state (not necessarily at steady state) ahead of the front. As the $b\ln(V^*\theta/D_c)$ term in (1) is sometimes written as Ψ [e.g., *Perrin et al.*, 1995], for shorthand we write (with no b)

$$\Psi_0(t) = \ln\frac{V_{\max}(t)\theta_{bg}}{D_c}. \tag{6}$$

In all our simulations, for both the aging and slip laws the slip speed ahead of the front is low enough that there is very little state evolution until the pulse tip (peak stress) arrives. Thus θ_{bg} is well defined. This is analogous to slide-hold-slide laboratory experiments in which the true sliding velocity upon reloading following a "hold" does not instantaneously track the load point velocity, but reaches that velocity with minimal evolution of θ. Neglecting this evolution introduces errors that seem comparable to those associated with the standard "small-scale-yielding" assumption of linear elastic fracture mechanics.

[11] For a crack tip propagating at quasi-static equilibrium, the energy for fracture is provided by the mechanical energy release rate G. When using superposition it is more convenient to work with stress intensity factors K, which add linearly. In that case the equilibrium condition equivalent to $G = G_c$ is $K = K_c$, where the fracture toughness K_c is related to G_c via $K_c^2 = 2\mu' G_c$ [*Lawn*, 1993]. Thus from (5),

$$K_c = (2\mu' b\sigma D_c \Psi_0)^{1/2}. \tag{7}$$

3. Numerical Slip Pulses

[12] Figure 1 shows snapshots of two styles of slip pulses observed by *Ampuero and Rubin* [2008]. Initial conditions are shown in red. In both examples the fault started below steady state ($V\theta/D_c < 1$) except for a localized asymmetric perturbation that reached steady state at $x = 0$. A small background loading rate was applied. The initial perturbation decayed more slowly to the left, such that a pulse initiated on the left and reached large slip speeds before a pulse developed on the right. Distances in Figure 1 are normalized by L_b, defined as

$$L_b = \frac{\mu' D_c}{b\sigma}. \tag{8}$$

L_b is the relevant length scale under the aging law when $V\theta/D_c \gg 1$ [*Dieterich*, 1992; *Rubin and Ampuero*, 2005]; the corresponding length scale at the front of the slip law pulse is L_b/Ψ_0 [*Ampuero and Rubin*, 2008]. Resolving the pulse front at large slip speeds requires a very fine grid spacing; as maximum values of Ψ_0 reach ~25, we used $L_b/180$.

[13] Note that the snapshots in Figure 1 are plotted at equal increments of $\log(V_{\max})$ and not time; the time intervals become dramatically shorter (very roughly as $D_c/V_{\max}$) as the pulse accelerates to instability. Because there is a unique relation between the maximum slip speed and the pulse propagation speed [*Ampuero and Rubin*, 2008] (see also equation (31)), the two pulses in Figure 1 have essentially the same propagation speed when compared at the same $V_{\max}$. Thus nucleation in Figure 1a is accelerating to instability more rapidly than in Figure 1b, in that the pulse propagates a shorter distance, at the same propagation speed, between neighboring values of $V_{\max}$.

[14] We refer to the length scale behind the tip over which significant slip is accumulating as the pulse width; reasonable values are $\sim 2L_b$ and $10L_b$ for the final snapshots in Figures 1c and 1d, respectively. For the pulse in Figure 1c the total slip remains approximately constant as the pulse width varies as Ψ_0^{-1}. Figure 2b shows that when distances are stretched by Ψ_0 the displacement profiles

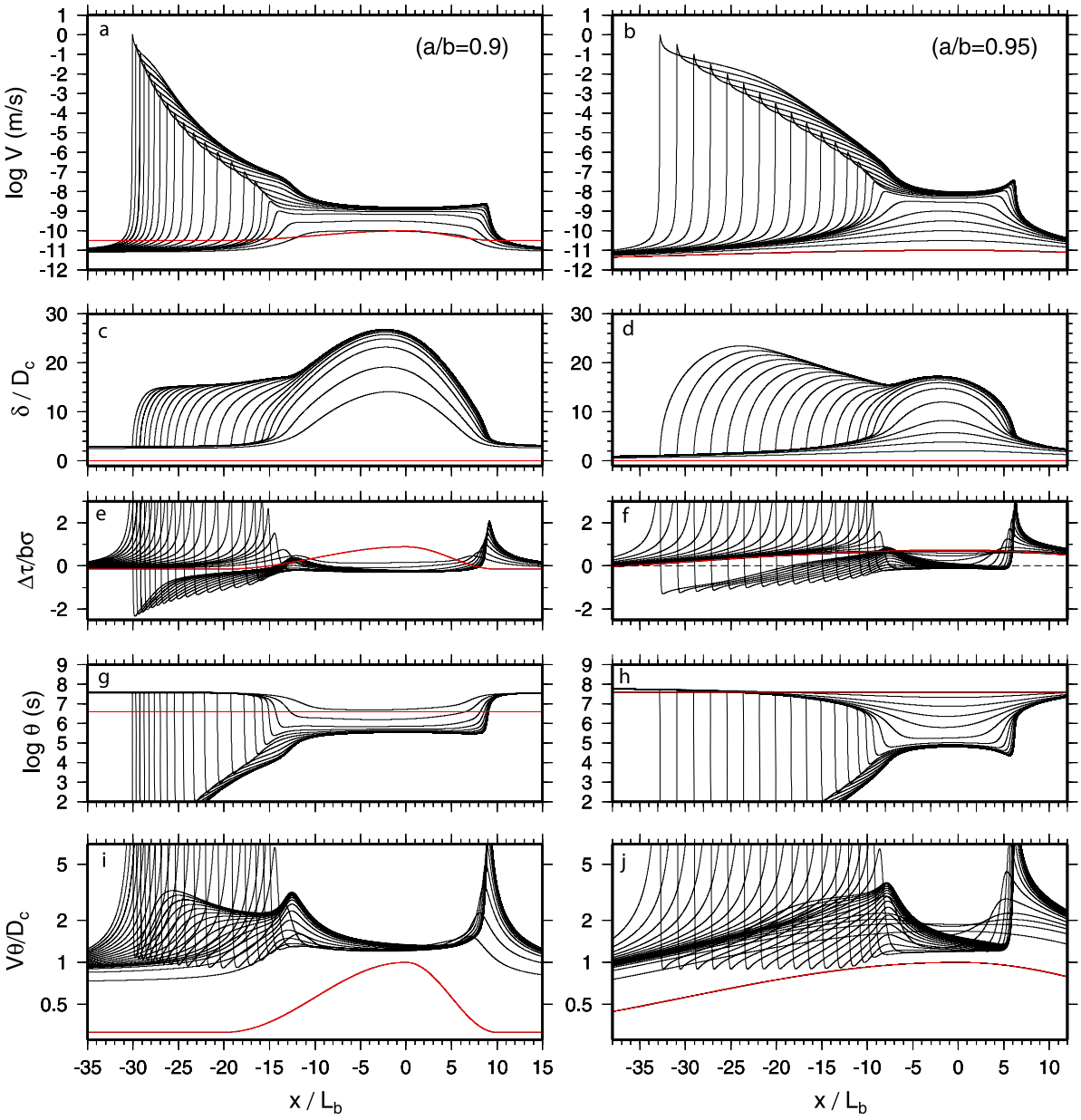

Figure 1. Snapshots of (a and b) slip speed, (c and d) normalized slip, (e and f) normalized stress drop, (g and h) state, and (i and j) proximity to steady state, as a function of normalized position for two styles of slip pulses observed by *Ampuero and Rubin* [2008]. Initial conditions are shown by the red curves, and values of a/b are specified in Figures 1a and 1b. The simulations are stopped when $V_{\max}$ reaches 1 m/s, somewhat beyond the limit of applicability of the quasi-static equations used.

appear to asymptotically approach a fixed distribution; this suggests that a self-similar solution might be found. For the pulse in Figure 1d, both the peak slip and the pulse width increase in proportion to Ψ_0, so when both axes are reduced by this quantity the displacement profiles again asymptotically approach a fixed distribution (Figure B1c). *Ampuero and Rubin* [2008, Figure 7] also observed a third style of pulse in which the pulse width varied relatively little while the peak slip increased roughly as $\Psi_0^{1/2}$ (see Figure B1d).

[15] For any given $V_{\max}$ the fracture energy is $b\sigma D_c \Psi_0$, independent of the pulse style. For a stress distribution $\Delta\tau$ acting over a distance L behind the tip of a semi-infinite crack, the mechanical energy release rate G, that must balance G_c, is dimensionally

$$G \sim \frac{L\Delta\tau^2}{\mu'} \tag{9}$$

[*Lawn*, 1993], while from elasticity

$$\Delta\tau \sim \mu' \frac{\delta}{L}. \tag{10}$$

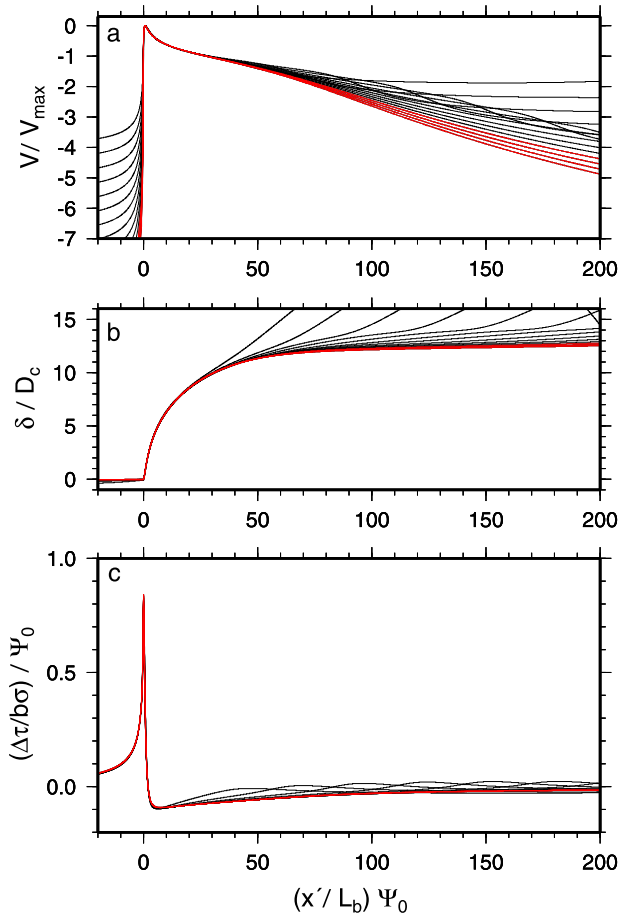

Figure 2. Snapshots of (a) slip speed normalized by the current maximum, (b) normalized slip, and (c) scaled normalized stress drop, as a function of scaled normalized distance behind the pulse tip, showing the approach to self-similarity for the slip pulse in Figures 1a, 1c, 1e, 1g, and 1i. The pulse tip is defined as the location of peak stress; slips in Figure 2b are relative to the slip at that point. All snapshots with maximum slip speeds $\geq 10^{-7}$ m/s are shown; red curves show the last four snapshots. At the time of the last snapshot $\Psi_0 = 25.3$, so a value of 50 on the horizontal axis in Figure 2 corresponds to a distance of roughly $2L_b$ behind the last pulse tip shown in Figure 1.

If we assume

$$\delta/D_c \propto \Psi_0^p, \tag{11}$$

where p is some growth exponent, then with $G = G_c \propto \Psi_0$ (equations (5) and (6)), equations (9) and (10) imply

$$\Delta\tau/b\sigma \propto \Psi_0^{(1-p)}; \tag{12}$$

$$L/L_b \propto \Psi_0^{(2p-1)}. \tag{13}$$

The pulses we have observed numerically correspond to $p = 0$ (Figure 1, left), $p = 1$ (Figure 1, right), and $p = 1/2$ (Figure B1, right). For example, in Figures 1e and 2c the maximum stress drop, reached just behind the tip, is proportional to Ψ_0, consistent with $p = 0$ (equation (12)).

[16] *Ampuero and Rubin* [2008] also noted that each style of pulse was associated with its own rate of acceleration to instability. Empirically their results are consistent with

$$\frac{\dot{V}_{\max} D_c}{V_{\max}^2} \propto \Psi_0^{-2p+1}, \tag{14}$$

where $\dot{V}_{\max} \equiv dV_{\max}/dt$. In Appendix B we will show that (14) follows from the observed self-similarity of the velocity profiles. For $p = 1/2$ (14) becomes $\dot{V}_{\max} D_c / V_{\max}^2 =$ const., the same as for all nucleation regimes under the aging law [*Dieterich*, 1992; *Rubin and Ampuero*, 2005]. In this case the time remaining to instability varies as $D_c/V_{\max}$. The larger value of the exponent in (14) for $p = 0$ than for $p = 1$ seems consistent with the more rapid approach to instability in Figure 1a than in Figure 1b, although buried in the implied proportionality constant is an unspecified dependence upon a/b and p that could also influence this.

[17] Coupled with the observation that $V\theta/D_c$ approaches steady state near the stress minimum behind the pulse tip (Figures 1i and 1j) [see also *Ampuero and Rubin*, 2008, Figure 7], equation (12) implies that the pulse style is closely tied to the ambient conditions along the fault. To see this, we can write $\Delta\tau_{\min} = \tau_{bg} - \tau_{\min}$, where τ_{bg} is the background stress and $\tau_{\min}$ the stress minimum. Manipulating (1) with the constraint of being at steady state at $\tau_{\min}$ with slip speed $\sim V_{\max}$ leads to

$$\frac{\Delta\tau_{\min}}{b\sigma} = \left(\frac{a}{b} - 1\right)\Psi_0 - \frac{a}{b}\Psi_{bg}, \tag{15}$$

where $\Psi_{bg} \equiv \ln(V_{bg}\theta_{bg}/D_c)$. Thus $\Delta\tau_{\min}$ will be proportional to Ψ_0 ($p = 0$ (Figure 1, left)) if the pulse propagates into a region initially at steady state ($\Psi_{bg} = 0$). For $\Delta\tau_{\min}$ to be constant, on the other hand ($p = 1$ (Figure 1, right)), equation (15) requires an a/b-dependent linear relation between $\Psi_{bg}(t)$ and $\Psi_0(t)$. Graphically, the ambient stress must decrease in the direction of pulse propagation in parallel with the steady state strength, as can be seen in Figure 1f. Such considerations provide insight into how the different initial conditions in Figure 1 gave rise to the different pulse styles observed. For the example in Figure 1 (left), the pulse propagated into a region outside the initial perturbation where Ψ_{bg} was quasi-constant and close to steady state. For the example in Figure 1 (right), the pulse propagated within the initial perturbation, in a region where Ψ_{bg} decreased quasi-linearly in the propagation direction.

[18] All three pulse styles exhibit the same scaling within the region of large strength loss immediately behind the pulse front [*Ampuero and Rubin*, 2008, Figure 10e]. The reason is that this strength loss is dominated by state evolution under conditions of near-constant slip speed, and this is a universal property of the evolution law. We

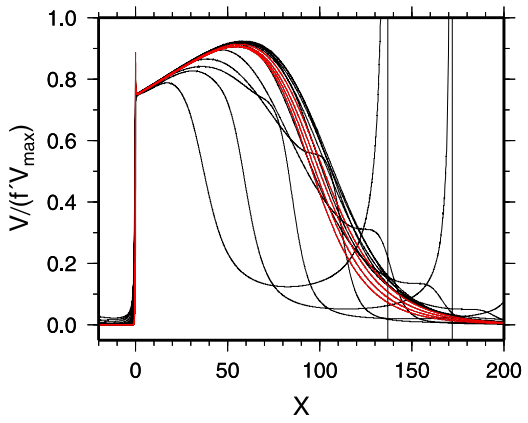

Figure 3. Snapshots of $V/f'V_{\max}$ for the snapshots of Figure 2, as a function of $X = (x'/L_b)\Psi_0$. If $V/V_{\max}$ is a function of X only, equation (18) implies collapse to a line of slope C. The "spike" at $X = 0$ comes from the error in determining the slip gradient f' via centered finite differences at the grid point closest to the pulse tip.

refer to this as the near-tip or slip-weakening region. Its length R is given dimensionally by

$$R \sim \delta_c \frac{\mu'}{\Delta\tau_{p-r}} = \delta_c \frac{\mu'}{b\sigma\Psi_0}, \tag{16}$$

where δ_c is the effective slip-weakening distance (roughly $2D_c$ for the slip law) and $\Delta\tau_{p-r} = b\sigma\Psi_0$ is the strength loss behind the front (evolution effect). Comparing the Ψ_0 dependence of (16) and (13) shows that the scaling of R is identical to that of the entire pulse only for $p = 0$. This makes deriving a self-similar solution simplest for that case. The assumption that the fault is initially at steady state also seems less contrived than requiring a particular gradient of the ambient stress, as seems necessary for $p = 1$. In sections 4 and 5 we derive a self-similar solution for $p = 0$; some generalizations to other values of p are given in Appendix B.

4. Implications of Self-Similarity With $p = 0$

[19] Figure 2b motivates writing the normalized slip as a function of scaled distance X behind the tip; that is,

$$\frac{\delta(x,t)}{D_c} = f(X), \quad X \equiv \frac{x'}{L_b}\Psi_0, \tag{17}$$

where x' is the physical distance behind the tip and the time dependence is now embodied in Ψ_0. Assuming a uniform θ_{bg} and differentiating (17) with respect to time (for details see Appendix A), the slip speed normalized by its current maximum is

$$\frac{V}{V_{\max}} = \frac{f'}{f'_{Vm}} + f'C(X - X_{Vm}). \tag{18}$$

Here $f' \equiv df/dX$, X_{Vm} is the scaled position of the maximum slip speed, f'_{Vm} is f' evaluated at X_{Vm}, and, consistent with equation (14) with $p = 0$, C characterizes the rate of acceleration to instability $\dot{V}_{\max}$:

$$C \equiv \frac{\dot{V}_{\max}}{V_{\max}^2}\frac{D_c}{\Psi_0}. \tag{19}$$

The first term in (18) would be the sole term for a steady state pulse; the second comes from the fact that the length scale changes with Ψ_0. We find numerically that because of the universality of the near-tip stress distribution, f'_{Vm} and X_{Vm} vary by only 5% as a/b increase from 0.8 to 0.95; for $a/b = 0.9$, $f'_{Vm} \sim 1.33$ and $X_{Vm} \sim 0.66$.

[20] Although self-similarity of the slip profiles as embodied in (17) does not require C = constant, if the profiles of $V/V_{\max}$ are also functions of X but not time, as in Figure 2a for small-to-moderate X, then from (18) C must be independent of time. We can test this by plotting $V/(V_{\max}f')$ versus X; from (18) the result should be a line of slope C. Figure 3 shows that the simulation of Figure 2 evolves to such a state over $0 < X \lesssim 50$, where the accumulated slip has reached roughly 90% of its ultimate value. That is, self-similarity of both the slip and velocity profiles is maintained over most of the pulse width but not farther from the tip. The value of C obtained from the slope is 0.0036, within a few percent of the value obtained by differentiating the numerical output to determine $\dot{V}_{\max}$ and then substituting the result into (19).

[21] If slip is a function of X alone, then from (2) we can write the normalized stress change as (see also Figure 2c)

$$\frac{\Delta\tau}{b\sigma} = \Psi_0 g(X). \tag{20}$$

The remainder of the derivation is somewhat cumbersome and not very illuminating, so we leave the details for Appendix A. The basic strategy is to substitute equations (18) and (20) for V and $\Delta\tau$ into equation (1) for the frictional strength to constrain θ. This requires first relating $\Delta\tau$ to τ via the background stress state, which is where the requirement of a steady state background enters the solution. Substituting the time derivatives of V and τ into the time derivative of (1) then constrains $\dot{\theta}/\theta$. Requiring this $\dot{\theta}/\theta$ to be consistent with the evolution law leads finally to equation (A16), which, after retaining only the dominant terms (those that multiply Ψ_0), becomes

$$C\left(g - \frac{a}{b}\right) + \left(\frac{g'}{f'} + g + 1 - \frac{a}{b}\right)\frac{V}{V_{\max}} = 0, \tag{21}$$

with $V/V_{\max}$ given by (18). Along with the elasticity equation (2) relating g to f', (21) becomes the governing equation for self-similar slip law slip pulses with $p = 0$. The conclusions in sections 4.1–4.5 follow directly from this, independent of the particular forms of f and g.

4.1. Spatial Extent of Self-Similarity

[22] For a constant displacement dislocation, the stress (and hence g) varies as X^{-1}, so g' varies as X^{-2}. In the limit of large X, equation (18) becomes $V/V_{\max} \approx f'/f'_{Vm} + f'CX$.

In this limit, then, retaining only the (possibly) nonzero terms in (21) leads to

$$\frac{a}{b} = \left(1 - \frac{a}{b}\right) f' X. \tag{22}$$

But f' must decay more rapidly than X^{-1} or the displacement will increase at least as ln X, so for large X (22) implies $a/b = 0$. Therefore (21) does not satisfy the expected boundary conditions for large X. This is consistent with Figure 3, which shows that self-similarity extends over most of the pulse width but no farther.

4.2. Stress Minimum

[23] The stress minimum behind the tip can be determined by setting $g' = 0$ in (21), leading to

$$g_{\min} = \left(\frac{a}{b} - 1\right) + \frac{C}{C + V_{g\min}/V_{\max}}, \tag{23}$$

where $V_{g\min}$ is the slip speed evaluated at the stress minimum. In all our simulations $V_{g\min}/V_{\max}$ is of order 1 (numerically we find it to be ~ 0.3, regardless of p or a/b), while C in the example in Figure 3 is 2 orders of magnitude lower. In section 5 we estimate C to be $\sim 0.4(1 - a/b)^2$, implying that the second term on the right in (23) is smaller than the first by a factor of $\sim (1 - a/b)$. Thus for a/b near 1,

$$g_{\min} \approx -(1 - a/b), \tag{24}$$

explaining why $g_{\min} \sim -0.1$ in Figure 2c. To the extent that $\ln(V/V_{bg})$ can be approximated as constant from $V_{\max}$ to $V_{g\min}$, (24) also implies that the fault is near steady state at the stress minimum. This follows from equation (1) and the definition $g \equiv \Delta\tau/b\sigma\Psi_0$ (equation (20)); for a fault initially at steady state subjected to a constant velocity $V_{\max}$ the change in steady state stress is $(a/b - 1)b\sigma\Psi_0$. In Appendix D we show why this stress minimum is also approximately a minimum in $\ln(V\theta/D_c)$ (Figures 1i and 1j).

4.3. Dependence Upon a/b

[24] Although $g_{\min}$ varies with a/b, the fracture energy does not (equation (5)). Thus larger magnitudes of $g_{\min}$ must be compensated for by smaller length scales L over which those stresses act. With $G \sim L\Delta\tau^2/\mu'$ (equation (9)), $\delta \sim L\Delta\tau/\mu'$ (equation (10)), and $\Delta\tau/b\sigma \propto (1 - a/b)$ (equation (24)), we anticipate

$$\delta/D_c \propto (1 - a/b)^{-1}; \tag{25}$$

$$L/L_b \propto (1 - a/b)^{-2}. \tag{26}$$

These scalings are properties of the analytical solution derived in section 5. To estimate the dependence of C upon a/b requires estimates of f and g in (21).

4.4. Time to Instability

[25] Under the aging law, expanding nucleation zones accelerate to instability according to

$$\frac{\dot{V}}{V^2} = \frac{C_{age}}{D_c}, \tag{27}$$

where the constant $C_{age} = (\pi/2)(1 - a/b)$ and V is the quasi-uniform slip speed within the interior of the nucleation zone [*Rubin and Ampuero*, 2005]. Neglecting elastodynamics, infinite slip speeds are reached at a finite time t^* given by

$$t^* - t = \frac{D_c}{C_{age} V(t)}. \tag{28}$$

Inspection of equations (27) and (19) shows that, given comparable values of the constant, instability is reached sooner for the slip law with $p = 0$ than for the aging law. An analytic solution for equation (19) shows that in the limit of large Ψ_0, the time remaining to instability is

$$t^* - t \approx \frac{D_c}{C\Psi_0(t) V_{\max}(t)} \tag{29}$$

(Appendix B). This result might be rationalized by noting that for large $V_{\max}$, $d\Psi_0/dV_{\max}$ tends to zero, so Ψ_0 acts as a quasi-constant correction to C. Once C is known, $\Psi_0(t)$ and $V_{\max}(t)$ can be determined by solving equation (B17) numerically.

4.5. Propagation Distance

[26] Writing $dV_{\max}/dt$ as $(dV_{\max}/dl)(dl/dt)$, where l is the position of the pulse tip, equation (19) becomes

$$\frac{dV_{\max}}{dl}\frac{dl}{dt} = \frac{C}{D_c}\Psi_0 V_{\max}^2. \tag{30}$$

Ampuero and Rubin [2008] showed that for both the aging and slip laws the propagation speed $V_{prop} = dl/dt$ satisfies

$$V_{prop} = V_{\max}\frac{L_b}{D_c}\frac{1}{f'_{Vm}\Psi_0}. \tag{31}$$

This is because to first order the front of the slip pulse propagates with a steady state slip profile, so that the slip speed is simply the propagation speed times the local slip gradient (with regard to equation (A6), the second term within brackets, which accounts for the sharpening of the pulse front, is less than a few percent of the first, which accounts for its steady state translation). The slip gradient is determined largely by the near-tip strength loss $b\sigma\Psi_0$, with a/b and p having only a few percent influence on f'_{Vm} (even changing between the slip and aging laws alters f'_{Vm} by only $\sim$20%). Substituting (31) into (30) leads to

$$\frac{d\Psi_0/d\bar{l}}{\Psi_0^2} = f'_{Vm} C, \tag{32}$$

where $\bar{l} \equiv l/L_b$. As this equation is identical in form to (27), instability (infinite Ψ_0) is reached at a finite location $\bar{l}^*$ given by

$$\bar{l}^* - \bar{l} = \frac{1}{f'_{Vm} C\Psi_0(\bar{l})}. \tag{33}$$

[27] Note that the expression for the time to instability (29) has V_{max} in the denominator, whereas (33) has only its logarithm (in Ψ_0). This means that if a slip pulse begins at $t = 0$ with $V_{max} = 10^{-8}$ m/s, then when $V_{max} = 0.1$ m/s the time remaining to instability is less than 10^{-7} of the pulse lifetime. In practical terms this means that for evaluating t^* it is immaterial whether one defines instability to occur at infinite slip speed or just elastodynamic slip speeds, a fact exploited by *Dieterich* [1994] to derive simplified expressions for earthquake aftershock rates. The same cannot be said for l^*; the distance remaining to instability at $V_{max} = 0.1$ m/s in Figure 1a ($\Psi_0 = 23.0$) is 25% of the distance remaining when $V_{max} = 10^{-8}$ m/s ($\Psi_0 = 5.8$). This contrast with t^* is even more stark for other values of p; for $p \geq 1/2$ instability is reached at a finite t^* but not a finite l^* (Appendix B). For example, dV_{max}/dl is constant in Figure 1b ($p = 1$), so l^* does not exist but the pulse obviously reaches elastodynamic slip speeds at a finite l.

5. Analytical Approximation for a Finite-Width Pulse

[28] To evaluate the remaining time or distance to instability it is still necessary to estimate the constant C in equations (29) or (33). To this end we must determine $f(X)$, $g(X)$, and their derivatives in (21). Examination of Figures 2c and 2b suggests that the slip pulses we seek to describe might reasonably be approximated as having a constant stress gradient over a finite-width pulse, with constant slip at greater distances from the tip. Given the rather abrupt onset of slip near the pulse front (50% of the total accrues over less than 10% of the pulse width), a constant stress gradient is a plausible smoothing of the $1/X$ singularity associated with a dislocation. Although the slip speed at large distances in Figure 2a is not zero, it is too low for significant additional displacements to accumulate prior to instability, so continued slip there does not influence the active pulse. Such a model has 4 parameters: The average stress change $\Delta\bar{\tau}$ and stress gradient $\nabla\tau$ within the pulse, the pulse width $2w$, and the total displacement D. To determine these we have the following 4 constraints (for details see Appendix C):

[29] 1. $K = K_c$ at $x = 0$:

$$\frac{1}{2\pi^{1/2}}\frac{D\mu'}{w^{1/2}} - \pi^{1/2}\Delta\bar{\tau}w^{1/2} + \frac{\pi^{1/2}}{2}\nabla\tau w^{3/2} = (2\mu' b\sigma D_c\Psi_0)^{1/2}. \tag{34}$$

The first term on the left represents the contribution to the stress intensity factor from a fixed displacement D for $x > 2w$ and zero stress change over $0 < x < 2w$, the second the contribution from a constant (negative) stress change $\Delta\bar{\tau}$ over $0 < x < 2w$, and the third the contribution from a constant stress gradient with zero average over $0 < x < 2w$ [*Broberg*, 1999]. The term on the right is K_c from (7).

[30] 2. $K = 0$ at $x = 2w$:

$$-\frac{1}{2\pi}\frac{D\mu'}{w^{1/2}} - \Delta\bar{\tau}w^{1/2} - \frac{1}{2}\nabla\tau w^{3/2} = 0. \tag{35}$$

The terms on the left have the same sources as those in (34).

[31] 3. Continuity of the stress gradient at $x = 2w$: The constraint $K = 0$ ensures that the stress remains finite, but permits a cusp in the stress distribution at $x = 2w$ that for the adopted friction law seems unphysical. A continuous stress gradient requires

$$\nabla\tau = -\frac{\Delta\bar{\tau}}{2w}; \tag{36}$$

that is, the difference in stress between the pulse endpoints has the same magnitude as the average stress drop.

[32] 4. From (24) and (20), the stress at the tip is

$$\Delta\tau_{min} = -b\sigma\Psi_0\left(1 - \frac{a}{b}\right). \tag{37}$$

[33] Combining (34)–(37) leads to

$$\frac{D}{D_c} = \frac{9}{8}\left(1 - \frac{a}{b}\right)^{-1}, \tag{38}$$

$$g' = \frac{8\pi}{27}\left(1 - \frac{a}{b}\right)^{3}, \tag{39}$$

$$\frac{w}{L_b}\Psi_0 \equiv W = \frac{9}{8\pi}\left(1 - \frac{a}{b}\right)^{-2}, \tag{40}$$

where W is the scaled dimensionless version of w; in units of X, the pulse width is $2W$. Together with equation (24), $g_{min} = -(1 - a/b)$, this completes the solution. The slip over $0 < X < 2W$ and stress for $X > 2W$ can be determined by elasticity (Appendix C). For $a/b = 0.9$, (38)–(40) yield $D = 11.25D_c$, $g' = 0.93 \times 10^{-3}$, and $2W = 71.6$. For D and g' these are encouragingly close to the numerical values of $\sim 12.5D_c$ and $\sim 0.9 \times 10^{-3}$ for the example in Figure 2. The pulse width in the numerical simulations is subjective, as the slip gradient never reaches zero for large X, but from Figures 2 and 3 a value of $2W \sim 70$ seems reasonable.

[34] To determine the rate of acceleration to instability, one can solve for C in (21) by writing $g_{min} + g'X$ for g, substituting (18) and (24) for V/V_{max} and g_{min}, and taking the limit $X \gg X_{Vm}$:

$$C = \frac{1}{f'_{Vm}}\left\{\frac{1 - g'X}{g'(1 + f'X)} - X\right\}^{-1}. \tag{41}$$

Because the finite-width pulse is only an approximation to (21), we cannot expect the right side of (41) to be independent of X. Nonetheless, to the extent that this approximation is valid it should vary only slightly over the central portion of the pulse. Writing $X = \beta W$, where ultimately we will choose β to be not too far from 1 (the pulse midpoint), we can write $f'(X) = (1 - a/b)f'_2(\beta)$, where the function $f'_2(\beta)$ can be evaluated from equation (C16). Substituting βW for X, $(1 - a/b)f'_2$ for f', and (39) and (40) for g' and W, (41) becomes

$$C = \frac{(1 - a/b)^2}{f'_{Vm}}\left[\frac{\beta f'_2 + (8\pi/9)(1 - a/b)}{3 - (9/8\pi)\beta^2 f'_2 - 2\beta(1 - a/b)}\right]. \tag{42}$$

This estimate is plotted as the solid line in Figure 4 for $X = W$ ($\beta = 1$; $f_2' = 2/3$), and as the dashed line for $X = 0.5W$ ($\beta = 0.5$; $f_2' = 3^{1/2}$), assuming $f_{Vm}' = 1.33$. The two curves are suitably similar. Note that as a/b approaches 1, C is asymptotically proportional to $(1 - a/b)^2$; $C = 0.18(1 - a/b)^2$ for $X = W$ (dotted line) and $0.23(1 - a/b)^2$ for $X = 0.5W$. Numerical values from sections 6 and 7 (red dots) are better approximated as $C \sim 0.4(1 - a/b)^2$, but equation (42) shows that the full dependence upon a/b is not so simple.

6. How Robust a Solution?

[35] To verify that self-similar pulses with the scaling of Figure 2 are not restricted to a very limited range of a/b or Ψ_0 (see Appendix A), we sought numerical examples for other values of a/b. As the most important requirement seems to be that the pulse propagate into a region previously sliding at a uniform steady state, we prescribed initial and boundary conditions where for $x > 0$ and $t = 0$ the fault was sliding at steady state with 10^{-11} m/s, and for $x \leq 0$ and all $t \geq 0$ it was forced to slide at 10^{-9} m/s. Although these conditions may seem unrealistic, our motivation is simply to generate numerical pulses that might be analogs for the pulse-like portion of the nucleation process seen in Figure 1a.

[36] Figure 5 shows examples with $a/b = 0.8$, 0.9, and 0.95. In each case pulse propagation for the first 4 or so snapshots is driven by the prescribed slip over $x < 0$. However, after about the 5th snapshot, or peak slip speeds in excess of 10^{-8}–10^{-7} m/s, the pulses become self-driven in that they propagate with negligible additional displacement over $x < 0$. In accordance with the model of section 5 the total slip is constant and proportional to $(1 - a/b)^{-1}$; the solid bars in Figures 5a and 5b show the expectation from equation (38).

[37] We can evaluate the rate of acceleration C from equation (19) by differentiating the numerical output to obtain $\dot{V}_{\max}$ (Figure 6). Although it turns out not to be strictly constant in these simulations, C varies by only 10–20% for slip speeds from 10^{-5} – 1 m/s (it varies by less for the example in Figure 1a). The values at 1 m/s are 25–50% larger than the estimates from equation (42) (Figure 4).

[38] To further assess the accuracy of the approximate self-similar solution, Figure 7 shows the last five slip and stress profiles from each of the numerical simulations in Figure 5, with axes scaled by D, $\Delta\tau_{\min}$, and W in equations (37)–(40). The pulse width is $X/W = 2$. The self-similar solution is shown by the dashed black curve; after accounting for the scaling of the axes this solution is independent of a/b. Note that the numerical differences between the 3 values of a/b are comparable to the discrepancy between any particular a/b and the analytical solution. The largest discrepancy occurs in the stress profiles near $X/W = 0$, because the stress singularity in the analytical solution is smoothed by the near-tip strength loss in the numerical simulations. We can make an improved estimate of the actual stress minima by evaluating the second term on the right of equation (23), which represents a higher-order correction to the value $-(1 - a/b)$ assumed analytically. As was noted in section 4.2, this correction is roughly $(1 - a/b)$ times the first term, so higher-order corrections would imply scaled stress minima in Figure 7b of roughly -0.8, -0.9, and -0.95 for $a/b = 0.8$, 0.9, and 0.95, respectively. While these are close to the actual values, one might expect (23) to be "exact" in the sense that it assumes only self-similarity and not any particular form for f and g. Inserting into (23) the relevant values from the numerical simulations for each a/b, the expected minima in Figure 7b are -0.78, -0.88, and -0.978. That the actual values are not identical to these is symptomatic of these slip pulses being not exactly self-similar.

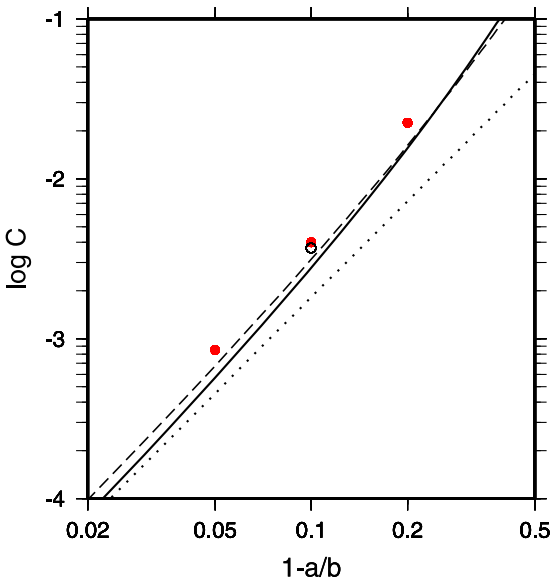

Figure 4. Solid curve shows the estimate of the acceleration constant C as a function of $(1 - a/b)$ determined by evaluating equation (42) at $X = W$; dashed curve shows the same but with (42) evaluated at $X = 0.5W$. Dotted line shows the asymptotic result for $a/b \sim 1$ corresponding to the solid curve. Red dots show the numerical values derived from evaluating the right side of equation (19) at $V_{\max} = 1$ m/s for the examples in Figure 5, and black circle shows the numerical value via the same method but for the example in Figure 2.

[39] Because the length of the slip-weakening region is nearly independent of a/b, that region occupies a larger fraction of the pulse as a/b (and hence W) decreases. For $a/b = 0.8$ this begins to impact the small-scale yielding approximation, which is presumably why the discrepancy between the numerical and analytical slip profiles for $X/W \lesssim 1$ is largest for this case (Figure 7a).

[40] To assess the importance of the assumption of a steady state fault, Figure 8 shows (from left to right) simulations with $V_{bg}\theta_{bg}/D_c = 4$, 2, 1.4, 1 (steady state), and 0.8. The slip magnitudes in these cases appear to be approaching their self-similar values, both with increasing Ψ_0 and with increasing proximity of $V_{bg}\theta_{bg}/D_c$ to steady state. Qualitatively this is consistent with the diminishing importance of the $\ln(V_{bg}\theta_{bg}/D_c)$ term in equation (A16), which was neglected in the self-similar solution. The propagation distances deviate more from the $p = 0$ self-similar solution than does the total slip, but as could have been anticipated this distance is shorter for $V_{bg}\theta_{bg}/D_c > 1$ (larger ambient stress) and longer for $V_{bg}\theta_{bg}/D_c < 1$. Because the propagation speed at a given $V_{\max}$ is essentially

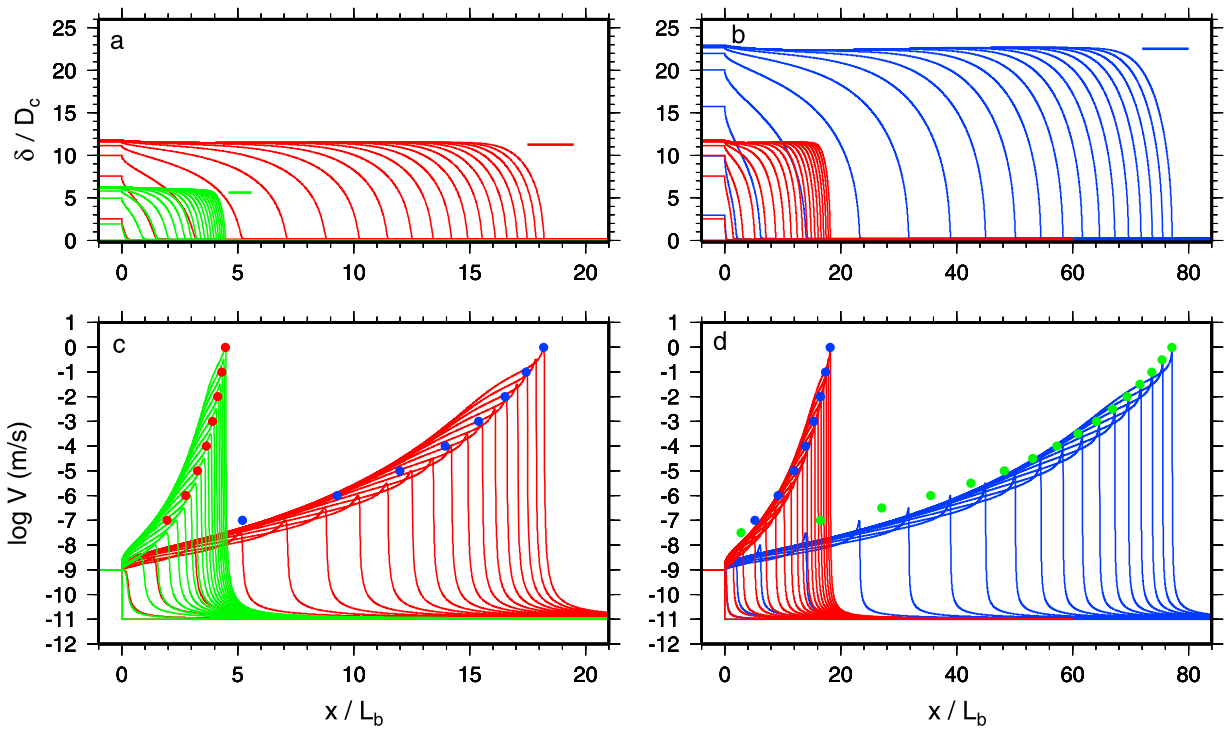

Figure 5. Examples of slip pulses where the fault was forced to slide at $V = 10^{-9}$ m/s for $x < 0$ and was initially sliding at steady state with $V = 10^{-11}$ m/s for $x \geq 0$. Green curves are for $a/b = 0.8$, red curves are for $a/b = 0.9$, and blue curves are $a/b = 0.95$. (a and b) The horizontal lines show the expected slip from (38). (c and d) The colored dots show the expected locations of the pulse front from (33), relative to the final snapshot, with C extracted from Figure 6 at $V_{max} = 1$ m/s.

fixed by Ψ_0 (equation (31)), a larger $d\ln(V_{max})/dl$ implies a larger $d\ln(V_{max})/dt$.

[41] This dependence upon the ambient state provides a qualitative explanation of Figure 7 of *Ampuero and Rubin* [2008], where an effective $V_{bg}\theta_{bg}/D_c$ of ~2 was reached via heterogeneous initial conditions. For each of $a/b = 0.8$, 0.9, and 0.95 in that figure the total slip is perhaps 75% of the $p = 0$ self-similar estimate, while the propagation distance is less than half that estimate.

7. Extrapolation to Natural Faults

[42] Even assuming that the slip law accurately describes state evolution in the presence of high temperatures and pore fluids, the pulses described here might operate only within a limited velocity range or be bypassed entirely, depending upon the ambient conditions. To place some bounds on $V_{bg}\theta_{bg}/D_c$, note that during rapid (elastodynamic) slip the fault is near steady state because the slip speed is quasi-constant for slip distances much larger than D_c. Immediately following the event the fault slows dramatically, so $V\theta/D_c \ll 1$ and $\dot{\theta} > 1$ (equation (4)). Because for $V\theta/D_c \ll 1$ the strength increase due to state evolution is very small for the slip law, and only logarithmic with time for the aging law, the increase in θ alone cannot balance a quasi-linear increase in loading stress. Thus V increases as well as θ (equation (1)), and $V\theta/D_c$ increases during the interseismic period. Self-driven nucleation, on the other hand, requires both increasing slip speed and decreasing stress. From (1) this implies a decreasing θ, requiring $V\theta/D_c > 1$. Thus nucleation is associated with the passage of the fault through steady state from below, as is true of both nucleation zones in Figure 1.

[43] Under 2 circumstances this increasing $V\theta/D_c$ and localization can persist until instability, bypassing pulse formation entirely: For a/b well below lab values [*Ampuero and Rubin*, 2008], and for rapidly increasing stresses, such

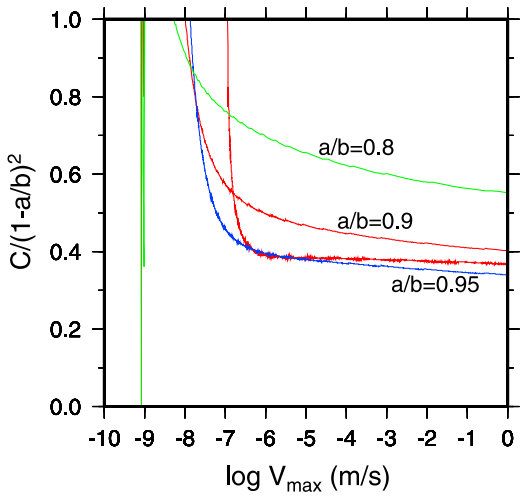

Figure 6. Plots of C as a function of V_{max} from the simulations in Figure 5, normalized by $(1 - a/b)^2$, determined from equation (19) by differentiating the numerical output to obtain $\dot{V}_{max}$. Red curve that is nearly constant for $V_{max} \gtrsim 10^{-6}$ m/s is from the simulation in Figure 1a ($a/b = 0.9$).

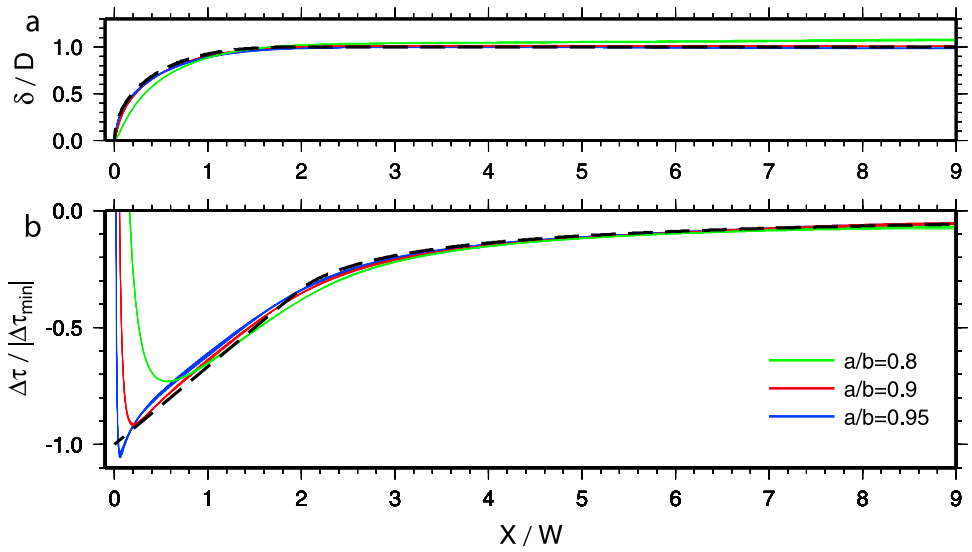

Figure 7. Comparison of the analytical finite pulse approximation (dashed line) to the last five snapshots from the numerical simulations in Figure 5. Pulse width is $2W$. (a) Slip normalized by D from (38). (b) Stress drop normalized by $\Delta\tau_{\min}$ from (37).

as occur following a nearby earthquake [*Kaneko and Lapusta*, 2008], or when creep fronts collide, for example within an asperity loaded by creep of the surroundings [*Chen and Lapusta*, 2009]. However, for lab values of a/b and low stressing rates, the stiffness of such a localized zone is too large to allow instability, causing $V\theta/D_c$ to decrease toward steady state and the nucleation zone to expand. The slip speed at the onset of expansion is sensitive to the initial conditions, in a way that we cannot yet predict quantitatively. All we can say at present is that in the simulations carried out thus far, the pulse develops at slip speeds that are orders of magnitude below elastodynamic. Unpublished numerical simulations demonstrate that this occurs also in 3-D, where the pulse may emanate from either the mode II or the mode III margins of the initially localized nucleation zone.

[44] Thus when a pulse develops, it emanates from a region that is somewhat above steady state (or localization

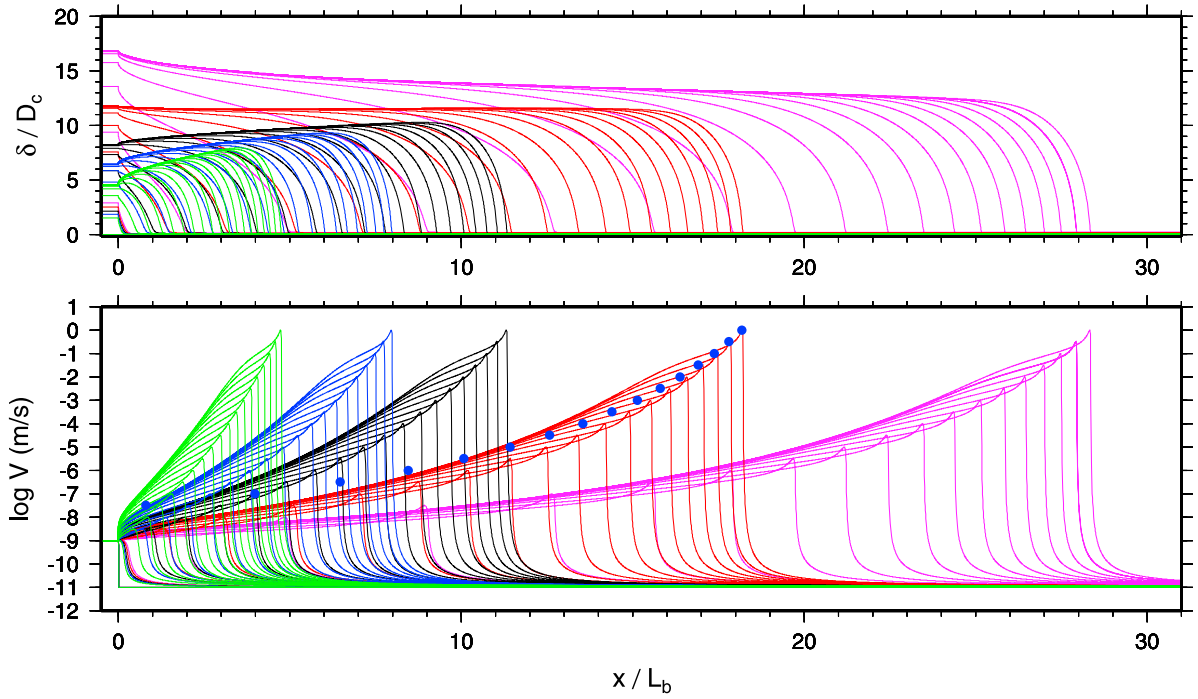

Figure 8. Examples of slip pulses with $a/b = 0.9$ where the fault was forced to slide at $V = 10^{-9}$ m/s for $x < 0$ and where initially $V = 10^{-11}$ m/s for $x \geq 0$. From left (green curves) to right the initial values of $V_{bg}\theta_{bg}/D_c$ were 4 (above steady state), 2, 1.4, 1, and 0.8 (below steady state). (top) Normalized slip. (bottom) Log slip speed.

would not have occurred), but not too far above steady state (or localization would have continued), as in Figure 1. We would not expect the adjacent fault to be farther above steady state or localization would have first occurred there. Conceivably the adjacent fault could be far below steady state, but given that it is contiguous with the original nucleation zone and was being stressed during that phase of nucleation, this would require a significant and abrupt change in material properties or ambient stress. Barring that, the fault into which the pulse propagates seems most likely to be slightly closer to steady state than the original zone of localization, as in Figure 1. In this sense the range of initial conditions explored in Figure 8 seems appropriate.

[45] At high slip speed, the slip pulses described here will be limited by the onset of elastodynamics if not sooner. Possibilities for "sooner" include pore fluid pressurization [*Segall and Rice*, 2006] or a high-speed cutoff to the evolution of state in the presence of hot pore fluids [*Nakatani and Scholz*, 2006]. Based on the acceleration-in-place, aging law nucleation model of *Dieterich* [1992], Segall and Rice suggested that thermal pressurization might dominate rate-and-state weakening at sip speeds as low as 10^{-5} m/s. Given how different these slip pulses are from Dieterich's model, however, with relatively little total slip occurring in regions that were only recently added to the pulse front, it is worth revisiting this issue. Nakatani and Scholz propose that under hydrothermal conditions, pressure solution creates relatively large, low-stress contact points that under stationary contact increase their area only slowly (compared to dislocation motion at high-stress contacts in room temperature experiments). When the characteristic time for a significant increase in contact area is larger than the contact age $\sim D_c/V$, evolution is not significant. The implications of such a constitutive law for nucleation on deformable faults have yet to be assessed.

8. Comparison to Aging Law Nucleation

8.1. Time to Instability

[46] For lab values of a/b and low stressing rates, nucleation zones following either the aging or the slip evolution law undergo expansion while $V\theta/D_c$ in the interior remains slightly above steady state. The difference is that this expansion takes the form of slip pulses under the slip law and cracks under the aging law. For the aging law in the crack expansion regime the time to instability is given by equation (28) with $C_{age} = (\pi/2)(1 - a/b)$ [*Rubin and Ampuero*, 2005]. Comparison to equation (29), with $f'_{Vm} \sim 1.33$ and $C \sim 0.4(1 - a/b)^2$, shows that instability occurs sooner for the slip law only if

$$\Psi_0 \gtrsim \frac{4}{1 - a/b} \frac{V^{age}}{V^{slip}_{\max}}, \tag{43}$$

where V^{age} is the quasi-uniform slip speed within the interior of the aging law nucleation zone. Given that in practical terms the maximum Ψ_0 is bounded by the onset of elastodynamics, (43) implies that for $V^{age} = V^{slip}_{\max}$, instability occurs sooner for the aging law if a/b is close to 1. This results from the different dependencies of (28) and (29) on $1 - a/b$, and it might seem surprising, given the smaller fracture energy implied by the slip law. However, *Ampuero and Rubin* [2008, equation B13] noted that for aging law nucleation zones the ratio of V in the interior to $V_{\max}$ at the margins is roughly proportional to $1 - a/b$, so that if a comparison is made at the same $V_{\max}$ the dependency of the 2 laws on a/b is approximately the same. Inserting into (28) their numerical values for the aging law of $V_{\max}/V \sim 6$ for $a/b = 0.9$ and $V_{\max}/V \sim 14$ for 0.95, instability occurs sooner for the slip law if $\Psi_0 \gtrsim 6$, or $V_{\max}/V_{bg} \gtrsim 400$. This comprises most or all of the region where C_{age} in (28) is expected to be accurate.

8.2. Nucleation Zone Size

[47] In the crack expansion regime the asymptotic nucleation length $2L_\infty$ for the aging law is

$$\frac{2L_\infty}{L_b} = \frac{2}{\pi}(1 - a/b)^{-2} \tag{44}$$

[*Rubin and Ampuero*, 2005]. Given that C in (33) is roughly proportional to $(1 - a/b)^2$, this length and the slip law propagation distance have roughly the same dependency upon a/b. If we take $V_{bg} = 10^{-11}$ m/s, and assume for example that a pulse develops at $V_{\max} = 10^{-8}$ m/s and reaches elastodynamic speeds at $V_{\max} = 10^{-2}$ m/s, then from (33) the propagation distance is roughly 1/6 the aging law nucleation length $2L_\infty$. For a fault initially above steady state that propagation distance can be significantly less (by more than a factor of 2 for $V_{bg}\theta_{bg}/D_c = 2$ in Figure 8). For the aging law, being initially above steady state can also reduce the nucleation size at elastodynamic speeds, but the effect is much more modest. For example, in Figure 1e of *Rubin and Ampuero* [2005], $V_{bg}\theta_{bg}/D_c \sim 3$ and the nucleation length at dynamic slip speeds is $\sim 75\%$ of $2L_\infty$.

8.3. Detectability

[48] The disparity between the two laws is even greater when one considers the size of the actively slipping region. While this can approach the full $2L_\infty$ for the aging law, for the slip law the slip speed has already dropped below $0.1V_{\max}$ by the pulse half-width w (Figure 2a, where $w = 32X$). From equations (40) and (44) the ratio $2L_\infty/w \sim 2\Psi_0$, which can easily reach a value of 40 at elastodynamic speeds [see also *Ampuero and Rubin*, 2008, Figure 2]. Thus the seismic signal from the final stages of nucleation is expected to be much smaller for the slip law than for the aging law. Unpublished simulations show that in 3-D this difference would be even greater, because while the aging law nucleation length is roughly $2L_\infty$ in both dimensions, for the slip law the length in the direction orthogonal to the 2-D simulations presented here is several times smaller than L_∞.

8.4. Total Slip

[49] Integrating (27) with $C_{age} = (\pi/2)(1 - a/b)$, the slip that accumulates between slip speeds V_1 and V_2 for the aging law is

$$\frac{\delta}{D_c} = \frac{2}{\pi}(1 - a/b)^{-1} \ln\frac{V_2}{V_1}. \tag{45}$$

As this has the same dependence upon a/b as does D for the slip law, we can ask how large a velocity increase is

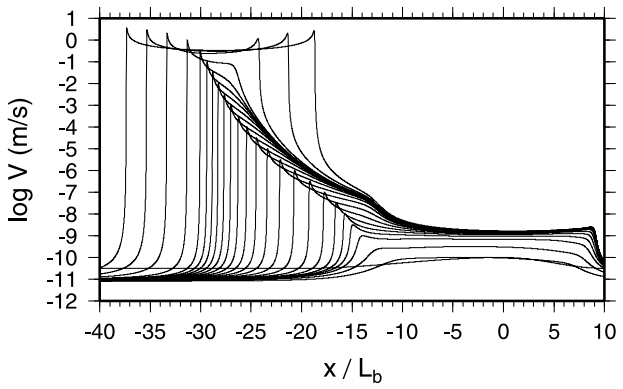

Figure 9. Snapshots from a simulation identical to that in Figure 1a except for the addition of radiation damping, meaning that the term $V\mu/2c_s$ has been added to the right side of equation (1), where μ is the shear modulus and c_s is the shear wave speed [*Rice*, 1993]. Radiation damping is expected to become important when the slip speed exceeds a value $V_{dyn} \sim 2a\sigma\beta/\mu$ [*Rubin and Ampuero*, 2005], which is roughly 0.6 m/s in this example. Snapshots are plotted at every half-magnitude increase in $V_{\max}$ until 1 m/s and then every $2L_b$ of propagation of the left front. When acceleration of slip is slowed by dynamics, the quasi-static slip pulse gives rise to a bilateral rupture. The propagation speed of the right rupture front is larger than that of the left, even though its peak slip speed is slightly less, because the quasi-static phase of nucleation has made θ_{bg} to the right smaller (equation (31)).

required for the aging law to accumulate the total slip of the slip law pulse. Setting (45) equal to (38) leads to $\ln(V_2/V_1) = 9\pi/16$, or $V_2/V_1 = 5.9$. Thus the total slip during nucleation, which accrues over many orders of magnitude in V, is many times larger for the aging law than for the slip law.

8.5. Lack of Implications for Elastodynamic Slip Pulses

[50] Given their form, it is tempting to think of the slip pulses described here as potentially "jump-starting" elastodynamic slip pulses during earthquake rupture. But this seems not to be the case. Despite the fact that all the action appears to be happening at the pulse front, the region behind the front is still accelerating, just more slowly. When the maximum slip speed is large enough that acceleration is limited by elastodynamics, this allows slower regions behind the front to also accelerate to elastodynamic speeds. In simulations that include radiation damping as an approximation to full elastodynamics [*Rice*, 1993], this leads to bilateral ruptures emanating from the region where the tip first reached radiation damping speeds (Figure 9). Although they differ in detail, fully elastodynamic simulations share this property (Y. Kaneko and J.-P. Ampuero, manuscript in preparation, 2009). Both the observed quasi-static pulses and the lack of elastodynamic pulses are consistent with the results of *Perrin et al.* [1995], who found that the slip evolution law could not give rise to steady state slip pulses with a slip speed that decreased to zero at some finite distance behind the pulse front. Neither their steady state nor their zero slip speed criterion is met by the quasi-static pulses we describe, although in practical terms the slip speeds we observe well behind the pulse front are negligibly small.

9. Conclusions

[51] We have derived a self-similar solution for one of three styles of slip pulses observed in numerical simulations of earthquake nucleation on faults obeying the slip law for state evolution. The solution is for faults that are initially at steady state, but remains useful for initial conditions that depart modestly from this. The stress drop, total slip, and pulse width vary with a/b as $(1 - a/b)$, $(1 - a/b)^{-1}$, and $(1 - a/b)^{-2}$, respectively. With increasing $\Psi_0 = \ln(V_{\max}\theta_{bg}/D_c)$ the stress drop, total slip, and pulse width vary as Ψ_0, Ψ_0^0, and Ψ_0^{-1}. The dependence of the stress drop, slip, and length scales with $(1 - a/b)$ is the same as for nucleation under the aging evolution law, making direct comparison rather straightforward. The same is not true of the variation with Ψ_0. In particular, the continual sharpening of the pulse front under the slip law bears no similarity to nucleation under the aging law, and would make the moment rate at the final stages of quasi-static nucleation much smaller for the slip law. This difference ultimately derives from the smaller increase in fracture energy with slip speed under the slip law. If existing lab experiments are a legitimate guide to natural faults, then the slip law is a more appropriate constitutive law for nucleation than is the aging law. However, we may be far from understanding the appropriate constitutive law for natural faults.

Appendix A: Self-Similarity With p=0

[52] Motivated by the scaling apparent in Figure 2, we begin by assuming

$$\frac{\delta}{D_c} = f(X), \quad X \equiv \frac{x'}{L_b}\Psi_0; \tag{A1}$$

$$\frac{V}{V_{\max}} = h(X); \tag{A2}$$

where x' is distance behind the pulse tip and $\Psi_0 \equiv \ln(V_{\max}\theta_{bg}/D_c)$. For a pulse propagating into a region initially sliding at a uniform background state $d\theta_{bg}/dt = 0$, so

$$\frac{dX}{dt} = \frac{d(x'/L_b)}{dt}\Psi_0 + \frac{x'}{L_b}\frac{\dot{V}_{\max}}{V_{\max}}; \tag{A3}$$

$$\frac{V}{D_c} = \frac{df}{dX}\frac{dX}{dt} = f'\left[\frac{V_{prop}}{L_b}\Psi_0 + X\frac{\dot{V}_{\max}}{V_{\max}\Psi_0}\right]; \tag{A4}$$

where we have equated dx'/dt with the pulse propagation velocity V_{prop}, and have written f' for df/dX and $\dot{V}_{\max}$ for $dV_{\max}/dt$. Multiplying by $D_c/V_{\max}$,

$$\frac{V}{V_{\max}} = f'\left[\frac{V_{prop}}{V_{\max}}\frac{D_c}{L_b}\Psi_0 + X\frac{\dot{V}_{\max}D_c}{V_{\max}^2\Psi_0}\right]. \tag{A5}$$

At $V = V_{\max}$,

$$1 = f'_{Vm}\left[\frac{V_{prop}}{V_{\max}}\frac{D_c}{L_b}\Psi_0 + X_{Vm}\frac{\dot{V}_{\max}D_c}{V_{\max}^2\Psi_0}\right], \quad \text{(A6)}$$

where f'_{Vm} and X_{Vm} are the values of f' and X evaluated where $V = V_{\max}$. Substitution back into (A5) yields

$$\frac{V}{V_{\max}} = f'\left[\frac{1}{f'_{Vm}} + C(X - X_{Vm})\right]; \quad C \equiv \frac{\dot{V}_{\max}}{V_{\max}^2}\frac{D_c}{\Psi_0}. \quad \text{(A7)}$$

With $V/V_{\max}$ a function of X only (equation (A2)), C must be constant.

[53] In what follows we will also need expressions for $\dot{V}/V$ and $\dot{\tau}$. When the pulse slip speed is large enough that the background stressing rate is irrelevant, $\dot{\tau} = \dot{\Delta\tau}$. Differentiating (18) and (20) and applying the chain rule as above,

$$\frac{\dot{V}}{V} = \frac{V_{\max}}{D_c}\left[C(1+\Psi_0) + \frac{f''}{(f')^2}\frac{V}{V_{\max}}\right]; \quad \text{(A8)}$$

$$\frac{\dot{\tau}}{b\sigma} = \Psi_0\frac{V_{\max}}{D_c}\left[\frac{g'}{f'}\frac{V}{V_{\max}} + Cg\right]. \quad \text{(A9)}$$

[54] Thus far we have made use only of the statement of self-similarity (equations (A1) and (A2)) in the derivation of equations (A8) and (A9), and a general statement of elasticity in deriving (20). But from the friction law, specifying $\Delta\tau$ and V places constraints on θ. From (1) we have

$$\Delta\tau \equiv \tau - \tau_{bg} = a\sigma\ln\frac{V}{V_{bg}} + b\sigma\ln\frac{\theta}{\theta_{bg}}, \quad \text{(A10)}$$

where by V_{bg} and θ_{bg} we imply values prior to any significant perturbation from the approaching slip pulse. Manipulating the logarithms in (A10) leads to

$$\ln\frac{V\theta}{D_c} = \frac{\Delta\tau}{b\sigma} + \left(1 - \frac{a}{b}\right)\left[\ln\frac{V_{\max}}{V_{bg}} + \ln\frac{V}{V_{\max}}\right] + \ln\frac{V_{bg}\theta_{bg}}{D_c}. \quad \text{(A11)}$$

If the pulse propagates into a region at steady state the last term on the right is zero, but we retain it for now. Substituting into (A11) the kinematic description of $\Delta\tau$ from (20),

$$\ln\frac{V\theta}{D_c} = \Psi_0\left[g + \left(1 - \frac{a}{b}\right)\right] + \left(1 - \frac{a}{b}\right)\ln\frac{V}{V_{\max}} + \frac{a}{b}\ln\frac{V_{bg}\theta_{bg}}{D_c}. \quad \text{(A12)}$$

[55] In addition to the constraint on $\ln(V\theta/D_c)$ from (A12), differentiating (1) places a constraint on $\dot{\theta}/\theta$. Starting with

$$\dot{\tau} = a\sigma\frac{\dot{V}}{V} + b\sigma\frac{\dot{\theta}}{\theta} \quad \text{(A13)}$$

and inserting the kinematic constraints on $\dot{V}/V$ and $\dot{\tau}$ from (A8) and (A9),

$$\frac{\dot{\theta}}{\theta} = \Psi_0\frac{V_{\max}}{D_c}\left[C\left(g - \frac{a}{b}\right) + \frac{g'}{f'}\frac{V}{V_{\max}}\right] - \frac{a}{b}\frac{V_{\max}}{D_c}\left[C + \frac{f''}{(f')^2}\frac{V}{V_{\max}}\right]. \quad \text{(A14)}$$

We can now insist that this $\dot{\theta}/\theta$, obtained by combining the frictional strength with the assumption of self-similarity, be consistent with the state evolution law. Substituting equation (A12) for $\ln(V\theta/D_c)$ into the slip law (equation (4)),

$$\frac{\dot{\theta}}{\theta} = -\Psi_0\frac{V}{D_c}\left[g + \left(1 - \frac{a}{b}\right)\right] - \frac{V}{D_c}\left[\left(1 - \frac{a}{b}\right)\ln\frac{V}{V_{\max}} + \frac{a}{b}\ln\frac{V_{bg}\theta_{bg}}{D_c}\right]. \quad \text{(A15)}$$

Finally, equating (A14) with (A15) leads to

$$\Psi_0\left[C\left(g - \frac{a}{b}\right) + \frac{g'}{f'}\frac{V}{V_{\max}}\right] - \frac{a}{b}\left(C + \frac{f''}{(f')^2}\frac{V}{V_{\max}}\right) = -\Psi_0\left[g + \left(1 - \frac{a}{b}\right)\right]\frac{V}{V_{\max}} - \left(1 - \frac{a}{b}\right)\frac{V}{V_{\max}}\ln\left(\frac{V}{V_{\max}}\right) - \frac{a}{b}\frac{V}{V_{\max}}\ln\left(\frac{V_{bg}\theta_{bg}}{D_c}\right). \quad \text{(A16)}$$

[56] Equation (A16) has the form $\Psi_0 A_1(X) + B_1(X) = \Psi_0 A_2(X) + B_2(X)$, where the left side comes from the combination of self-similarity and the frictional strength, and the right side from the combination of self-similarity and the evolution law. Two interpretations seem consistent with Figure 2. The first is that there is a self-similar solution that satisfies (A16) exactly, and toward which the numerical simulation evolves. This requires $A_1 = A_2$ and $B_1 = B_2$. The second interpretation is that only $A_1 = A_2$, and that the numerical simulation approaches self-similarity more and more closely as Ψ_0 increases and the $\Psi_0 A(X)$ terms dominate (for a fault initially at steady state, $\Psi_0 = 7$ for a velocity jump of 3 orders of magnitude and 20 for a jump of 9 orders of magnitude).

[57] For the simulation in Figure 2 the numerical results show that within the strongly weakening region behind the pulse tip ($X \lesssim 4$), the $\Psi_0 A(X)$ terms dominate and to within several percent $A_1 \sim A_2$. But although these terms still dominate over $X \gtrsim 5$, it is only by a factor of 2 or so even for relatively large Ψ_0, and in this region both $A_1 \sim A_2$ and $B_1 \sim B_2$. For $X \lesssim 4$ the (small) $B(X)$ terms are far from equal, but their difference nearly cancels the (small) difference between the $\Psi_0 A(X)$ terms. This near-cancelation persists for $X \gtrsim 4$ as well. Thus, the full equation (A16) is satisfied to greater accuracy than either $A_1 = A_2$ or $B_1 = B_2$. This seemed to raise the possibility that the self-similarity observed in Figure 2 is limited to a particular range of Ψ_0, or perhaps even a particular range of a/b. However, Figure 5 demonstrates that this self-similarity is not so fragile. As $A_1 \sim A_2$ everywhere within the pulse but

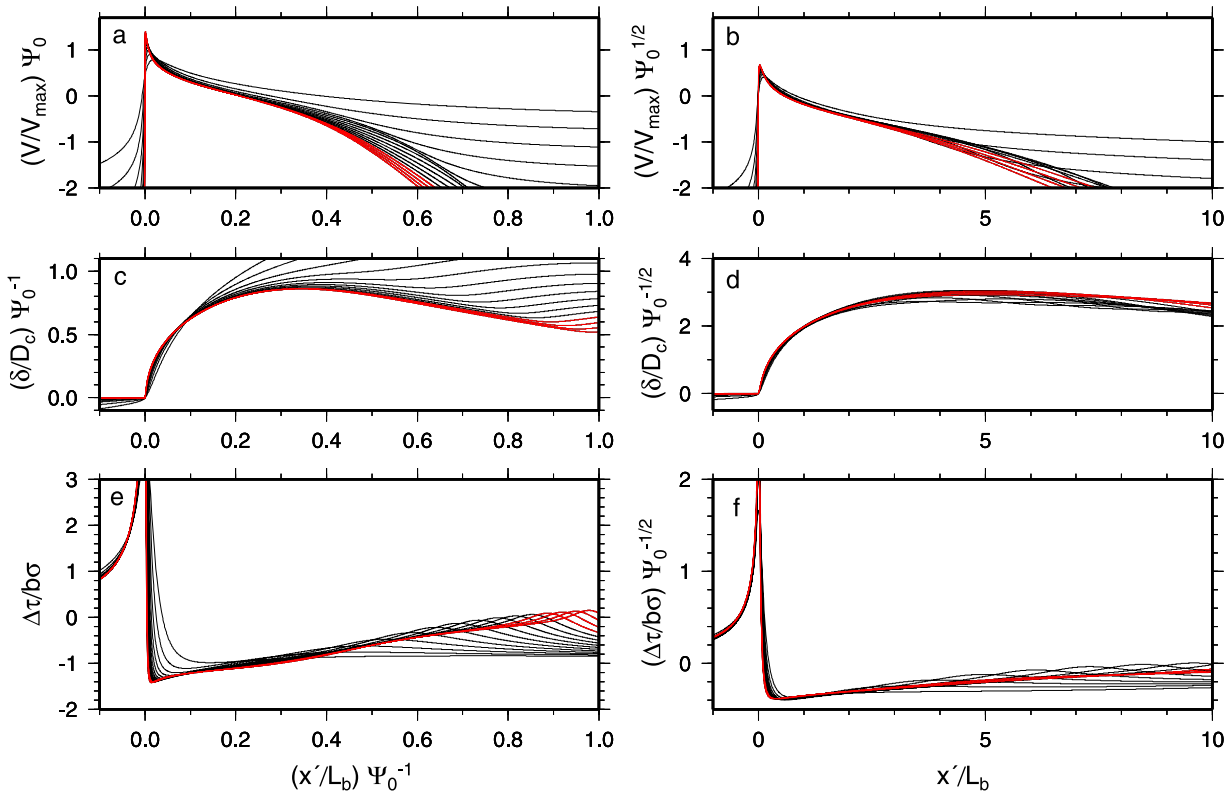

Figure B1. Snapshots of (a and b) normalized slip speed, (c and d) normalized slip, and (e and f) normalized stress drop, all scaled by the appropriate power of Ψ_0, as a function of scaled normalized position. Figures B1a, B1c, and B1e are for $p = 1$ (Figure 1, right), and Figures B1b, B1d, and B1f are for $p = 1/2$ [*Ampuero and Rubin*, 2008, Figure 7, right column]. In both cases, $a/b = 0.95$. Snapshots with $V_{\max}$ from 10^{-7} to 1 m/s are shown ($\Psi_0 = 6.2$–25.6 (Figure B1, left) and 6.6–22.7 (Figure B1, right)); the last four are in red. Scaling is consistent with equations (B1), (B2), and (B7).

$B_1 \neq B_2$ for $X \lesssim 4$, we set $A_1 = A_2$ to derive equation (21) in the main text.

Appendix B: Generalized Self-Similarity

[58] We noted in section 3 that only for $p = 0$ is the scaling of slip within the near-tip region the same as that within the bulk of the pulse. Here we develop some results for $p \neq 0$. Guided by the numerical simulations of *Ampuero and Rubin* [2008], we generalize (A1)–(A2) by hypothesizing self-similar solutions that on the scale of the pulse width, outside the near-tip region, satisfy

$$\frac{\delta}{D_c} = \Psi_0^p f(X), \quad X \equiv \frac{x'}{L_b}\Psi_0^{(1-2p)}; \tag{B1}$$

$$\frac{V}{V_{\max}} = \Psi_0^{-p} h(X). \tag{B2}$$

Examples satisfying (B1) and (B2) with $p = 1/2$ and 1 are shown in Figure B1. Note that $V_{\max}$ is the global maximum slip speed, which occurs in the near-tip region and which for $p \neq 0$ exceeds the maximum of the self-similar V in (B2).

[59] Evaluating dX/dt and df/dt as in (A3) and (A4), the generalization of (A5) (still neglecting $d\theta_{bg}/dt$ in comparison to $dV_{\max}/dt$) is

$$\frac{V}{V_{\max}} = \Psi_0^{-p}\left\{f'\left[\frac{V_{prop}}{V_{\max}}\frac{D_c}{L_b}\Psi_0 + (1-2p)CX\right] + pf\,C\right\}. \tag{B3}$$

where

$$C \equiv \frac{\dot{V}_{\max}}{V_{\max}^2}\frac{D_c}{\Psi_0^{(1-2p)}}. \tag{B4}$$

Ampuero and Rubin [2008] showed that for all p the near-tip scaling satisfies

$$\frac{V_{prop}}{V_{\max}}\frac{D_c}{L_b}\Psi_0 = \text{const} \equiv \frac{1}{f'_{Vm}}, \tag{B5}$$

so from (B3)

$$\frac{V}{V_{\max}} = \Psi_0^{-p}\left\{f'\left[\frac{1}{f'_{Vm}} + (1-2p)CX\right] + pf\,C\right\}. \tag{B6}$$

Thus self-similarity of V as in (B2) requires constant C, as verified by our simulations (Figure B2).

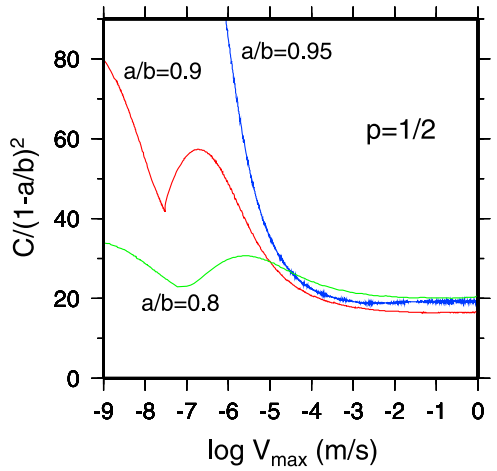

Figure B2. Plots of C as a function of V_{max}, determined by evaluating equation (B4) numerically, for three simulations with $p = 1/2$ and $a/b = 0.8$, 0.9, and 0.95 (those given by *Ampuero and Rubin* [2008, Figure 7]). As for the case $p = 0$, C is approximately proportional to $(1 - a/b)^2$, but the definition of C and the coefficient of proportionality differ.

[60] Because the maximum V in the self-similar solution does not match the global V_{max}, there is no trivial counterpart of (A6) or (A16). We can nevertheless obtain the following general results:

[61] Stress drop:

$$\frac{\Delta\tau}{b\sigma} = \Psi_0^{(1-p)} g(X). \tag{B7}$$

Propagation distance:

$$p \neq 1/2: \quad \Delta\bar{l} = \frac{1}{Cf'_{Vm}} \frac{\left[\Psi_0(\bar{l}_1)\right]^{-1+2p} - \left[\Psi_0(\bar{l}_2)\right]^{-1+2p}}{1-2p}; \tag{B8}$$

$$p = 1/2: \quad \Delta\bar{l} = \frac{1}{Cf'_{Vm}} \ln\frac{\Psi_0(\bar{l}_2)}{\Psi_0(\bar{l}_1)}; \tag{B9}$$

where $\Delta\bar{l} = (l_2 - l_1)/L_b$, with l the location of the pulse front. The derivation follows that in section 4.5. Only for $p < 1/2$ do the quasi-static equations give rise to infinite slip speeds at a finite l.

[62] Remaining time to instability:

$$p = 0: \quad t^* - t = \frac{D_c}{CV_{max}(t)\Psi_0(t)}; \tag{B10}$$

$$p = 1/2: \quad t^* - t = \frac{D_c}{CV_{max}}; \tag{B11}$$

$$p = 1: \quad t^* - t = (1+\Psi_0)\frac{D_c}{CV_{max}}; \tag{B12}$$

where t^* is the time of instability. To derive (B10), for example, write V_{bg} for D_c/θ_{bg} in equation (19) to obtain

$$\frac{\dot{V}_{max}}{V_{max}^2 \ln(V_{max}/V_{bg})} = \frac{C}{D_c}. \tag{B13}$$

This has the analytical solution

$$\mathrm{Ei}\left[-\ln\left(\frac{V_{max}(t)}{V_{bg}}\right)\right] - \mathrm{Ei}\left[-\ln\left(\frac{V_{max}(0)}{V_{bg}}\right)\right] = \frac{C}{D_c} V_{bg} t, \tag{B14}$$

where the exponential integral function Ei is defined as

$$\mathrm{Ei}(x) \equiv -\int_{-x}^{\infty} \frac{e^{-t}dt}{t}. \tag{B15}$$

For large x, $\mathrm{Ei}(x) \sim e^x/x$, so $\mathrm{Ei}[-\ln(x)] \sim -1/x\ln(x)$. This leads, for $\ln[V_{max}(0)/V_{bg}] = \Psi_0(0) \gg 1$ and $t \geq 0$, to (B10), with

$$t^* = \frac{D_c}{CV_{max}(0)\Psi_0(0)}. \tag{B16}$$

Combining (B16) with (B10), and recalling that $\Psi_0 \equiv \ln(V_{max}\theta_{bg}/D_c)$, the time history of V_{max} and Ψ_0 can be determined from the transcendental equation

$$V_{max}(t)\Psi_0(t) = \frac{V_{max}(0)\Psi_0(0)}{1 - t\dfrac{C}{D_c}V_{max}(0)\Psi_0(0)}, \tag{B17}$$

using the estimate of C from equation (42).

[63] Dependence upon a/b: Unlike the case $p = 0$, we have no analytical results for the dependence of the slip pulse attributes on a/b for $p = 1/2$ or 1. This can be traced to the lack of an equation equivalent to (24) for the stress minimum behind the tip. For all p it seems that the stress minimum is close to steady state with a slip speed near V_{max} (Appendix D); this is the constraint that led to equation (15). We can also write (B7) as

$$\frac{\Delta\tau_{min}}{b\sigma} = \Psi_0^{(1-p)} C_1\left(\frac{a}{b}, p\right), \tag{B18}$$

where the constant C_1 depends upon a/b and p. Equating (B18) with (15) leads to

$$C_1\left(\frac{a}{b}, p\right) = \left(\frac{a}{b} - 1\right)\Psi_0^p - \frac{a}{b}\frac{\Psi_{bg}}{\Psi_0^{(1-p)}}. \tag{B19}$$

For $p = 0$ and $\Psi_{bg} = 0$ this yields $C_1 = (a/b - 1)$, so (B19) is an alternate path to equation (24), the approximation to (23) that was used in obtaining the analytical self-similar solution. Equation (23), which takes full account of self-similarity between the pulse tip and the stress minimum, can then be thought of as a second-order correction to this. For the other p (B19) becomes

$$\Psi_{bg} = -\frac{(1-a/b)\Psi_0 + C_1\Psi_0^{1/2}}{a/b}, \quad p = 1/2; \tag{B20}$$

$$\Psi_{bg} = -\frac{(1-a/b)\Psi_0 + C_1}{a/b}, \quad p = 1. \tag{B21}$$

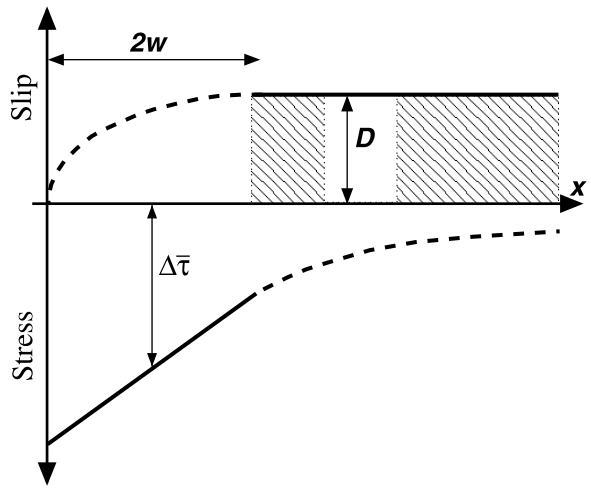

Figure C1. Schematic diagram for the superposition problem. Unknowns to be determined are the pulse width $2w$, the total slip D, and the average stress drop $\Delta\bar{\tau}$ and stress gradient $\nabla\tau$ within the pulse. The slip over $0 < x < 2w$ and stress for $x > 2w$ are then determined from elasticity.

Thus, equation (B19) emphasizes the point that the pulse style is dependent upon the ambient conditions along the fault. For $p = 1$, (B21) is permissive of but does not require that both Ψ_{bg} and Ψ_0 vary linearly with X, as seems to be approximately the case in Figure 1j. However, for both $p = 1/2$ and $p = 1$, additional information is needed to relate the unknowns C_1 and $\Psi_{bg}(X)$.

[64] Empirically, we find that the numerical simulations for $p = 1/2$ seem to show similar dependencies on a/b as for $p = 0$. For $p = 1/2$, C is even closer to proportional to $(1 - a/b)^{-2}$ than is the case for $p = 0$ (Figure B2). The same simulations indicate that the total slip, at a given Ψ_0, is approximately proportional to $(1 - a/b)^{-1}$, although not as precisely as for $p = 0$, and the pulse width, although difficult to identify precisely, varies roughly as $(1 - a/b)^{-2}$ [*Ampuero and Rubin*, 2008, Figure 8b].

Appendix C: Notes on the Finite-Width Pulse Solution

[65] We approximate the finite-width pulse as a crack with a constant stress gradient over $0 < x < 2w$, zero slip over $-\infty < x < 0$, and constant slip D over $2w < x < \infty$ (Figure C1). Our strategy is to superpose the following 3 fundamental solutions to obtain the desired boundary conditions. For convenience we introduce the coordinate transformation $\bar{x} = (x - w)/w$, so $-1 \le \bar{x} \le 1$ corresponds to $0 \le x \le 2w$.

[66] 1. Zero slip over $\bar{x} \le -1$, constant slip D over $\bar{x} \ge 1$, zero stress over $|\bar{x}| < 1$: The slip and slip gradient for $|\bar{x}| < 1$ are

$$\delta = \frac{D}{\pi}\left(\frac{\pi}{2} + \sin^{-1}\bar{x}\right), \tag{C1}$$

$$\frac{d\delta}{dx} = \frac{1}{\pi}\frac{D}{w}\frac{1}{\sqrt{1-\bar{x}^2}} \tag{C2}$$

[*Broberg*, 1999, section 4.4]. The stress over $|\bar{x}| > 1$, determined via the same techniques or by inserting (C2) into (2), is

$$\tau = -\frac{\mu'}{2\pi}\frac{D}{w}\frac{1}{\sqrt{\bar{x}^2-1}}\frac{\bar{x}}{|\bar{x}|}. \tag{C3}$$

[67] 2. Zero slip over $|\bar{x}| \ge 1$, uniform (negative) stress $\Delta\bar{\tau}$ over $|\bar{x}| < 1$:

$$\delta = -2w\frac{\Delta\bar{\tau}}{\mu'}\sqrt{1-\bar{x}^2}, \quad |\bar{x}| < 1; \tag{C4}$$

$$\frac{d\delta}{dx} = 2\frac{\Delta\bar{\tau}}{\mu'}\bar{x}\frac{1}{\sqrt{1-\bar{x}^2}}, \quad |\bar{x}| < 1; \tag{C5}$$

$$\tau = -\Delta\bar{\tau}\left[\frac{|\bar{x}|}{\sqrt{\bar{x}^2-1}} - 1\right], \quad |\bar{x}| > 1. \tag{C6}$$

[68] 3. Zero slip over $|\bar{x}| \ge 1$, $\tau = \nabla\tau\bar{x}$ over $|\bar{x}| < 1$: From *Secor and Pollard* [1975],

$$\delta = -\frac{\nabla\tau w}{\mu'}w\bar{x}\sqrt{1-\bar{x}^2}, \quad |\bar{x}| < 1; \tag{C7}$$

$$\frac{d\delta}{dx} = \frac{\nabla\tau w}{\mu'}\frac{2\bar{x}^2-1}{\sqrt{1-\bar{x}^2}}, \quad |\bar{x}| < 1; \tag{C8}$$

$$\tau = \nabla\tau w\left[\frac{1-2\bar{x}^2}{2\sqrt{\bar{x}^2-1}} + |\bar{x}|\right]\frac{\bar{x}}{|\bar{x}|}, \quad |\bar{x}| > 1. \tag{C9}$$

The slip contribution is negative for $\bar{x} > 0$.

[69] To satisfy the boundary conditions at $x = 2w$ (or $x = 0$) we write $\bar{x} = 1 + \bar{r}$ (or $\bar{x} = -1 - \bar{r}$), and examine the stresses as $\bar{r} \to 0^+$. For $\bar{x} \ge 1$, summing the 3 contributions leads to

$$\tau = -\frac{\mu'}{2\pi}\frac{D}{w}\frac{1}{\sqrt{\bar{r}}\sqrt{2+\bar{r}}} - \Delta\bar{\tau}\left[\frac{1+\bar{r}}{\sqrt{\bar{r}}\sqrt{2+\bar{r}}} - 1\right] + \nabla\tau w\left[-\frac{1+4\bar{r}+2\bar{r}^2}{2\sqrt{\bar{r}}\sqrt{2+\bar{r}}} + 1 + \bar{r}\right]. \tag{C10}$$

In the limit $\bar{r} \to 0$, and substituting r/w for $\bar{r}$,

$$\tau = \left[-\frac{D\mu'}{2\pi}w^{-1/2} - \Delta\bar{\tau}w^{1/2} - \frac{\nabla\tau}{2}w^{3/2}\right]\frac{1}{\sqrt{2r}}. \tag{C11}$$

Requiring finite stresses at $x = 2w$ means that the bracketed terms sum to zero; as they multiply $(2r)^{-1/2}$ these are (except for a factor of $\pi^{1/2}$) the respective stress intensity factors for the three loading styles listed in equation (35). The same analysis at $x = 0$ just reverses the sign of the first and third terms.

[70] With the $r^{-1/2}$ terms summing to zero (C10) becomes

$$\tau = -\Delta\bar{\tau}\left[\frac{\bar{r}^{1/2}}{\sqrt{2+\bar{r}}} - 1\right] + \nabla\tau w\left[-\frac{2\bar{r}^{1/2}+\bar{r}^{3/2}}{\sqrt{2+\bar{r}}} + 1 + \bar{r}\right]. \tag{C12}$$

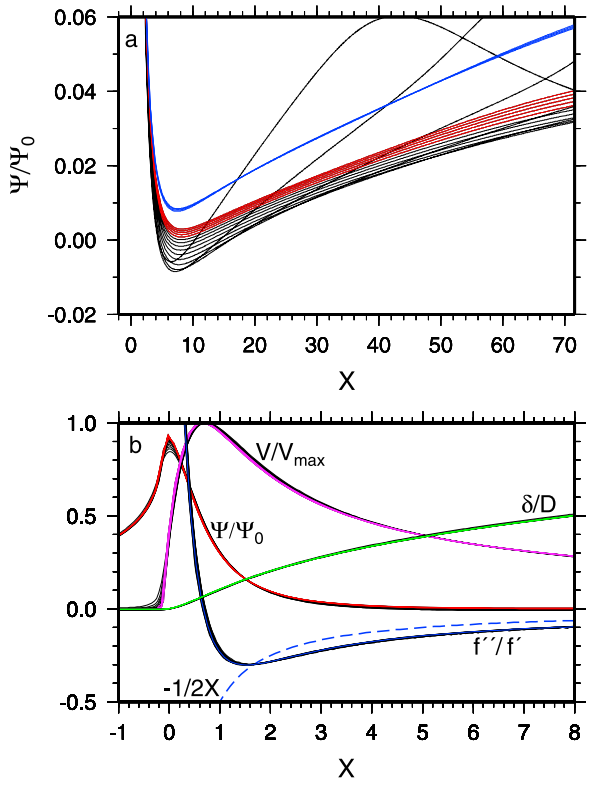

Figure D1. (a) Snapshots of $\ln(V\theta/D_c)/\Psi_0$ as a function of $X = (x'/L_b)\Psi_0$, over the pulse width $X \le 2W$, for the case $p = 0$, $a/b = 0.9$ in Figures 1 and 2. Snapshots from $V_{max} = 10^{-7}$ to 1 m/s ($\Psi_0 = 8.8$–25.3) are shown, with the last five in red. For comparison, the blue curves show the last five snapshots of $g + (1 - a/b)$, whose minimum as explained in section 6 differs from zero by roughly $(1 - a/b)^2$. For this and all other values of a/b and p, $V\theta/D_c$ has a minimum near steady state close to the minimum in $\Delta\tau$. (b) Snapshots, from $V_{max} = 10^{-7}$ to 1 m/s, of V/V_{max}, δ/D, Ψ/Ψ_0, f''/f', and for comparison $-1/2X$ (equation (D2)), as a function of X, in a zoom close to the pulse front.

Taking the derivative yields, in the limit $\bar{r} \to 0^+$,

$$\frac{d\tau}{dr} = -\frac{\Delta\bar{\tau}}{2\sqrt{2}w^{1/2}} r^{-1/2} - \frac{\nabla\tau w^{1/2}}{\sqrt{2}} r^{-1/2} + \nabla\tau. \tag{C13}$$

We would like $d\tau/dr$ for $r > 0$ to be continuous with the value $\nabla\tau$ specified as the boundary condition for $r < 0$. This requires that the $r^{-1/2}$ terms sum to zero, leading to

$$-\Delta\bar{\tau} = 2w\nabla\tau. \tag{C14}$$

[71] With these constraints we can solve for D, w, $\Delta\bar{\tau}$, and $\nabla\tau$ as described in the main text. Substituting the results (equations (37)–(39)) back into equations (C2), (C5), and (C8) and nondimensionalizing, we obtain the analytical expressions for f and f' used to approximate the slip and velocity distributions:

$$f = \frac{9}{8\pi}\left(1 - \frac{a}{b}\right)^{-1}\left[\frac{\pi}{2} + \sin^{-1}\overline{X} + \frac{4}{3}\sqrt{1-\overline{X}^2} - \frac{1}{3}\overline{X}\sqrt{1-\overline{X}^2}\right], \tag{C15}$$

$$f' = \frac{2}{3}\left(1 - \frac{a}{b}\right)\frac{1 - 2\overline{X} + \overline{X}^2}{\sqrt{1-\overline{X}^2}}, \tag{C16}$$

where $\overline{X} \equiv (X - W)/W$. Note that with $f'(2W) = 0$ this solution still violates the boundary condition at $X = 2W$ stipulated by equation (21).

Appendix D: Behavior of $V\theta/D_c$ Near the Stress Minimum

[72] We are interested in understanding why $V\theta/D_c$ has a minimum near steady state behind the pulse tip. First note that equation (A11) for $\ln(V\theta/D_c)$ makes no assumption about self-similarity. Because the last term on the right is zero and $\ln(V_{max}/V_{bg})$ varies with time but not X, to the extent that $\ln(V/V_{max})$ varies little relative to $\Delta\tau/b\sigma$ we expect that $\ln(V\theta/D_c)$ is just offset from $\Delta\tau/b\sigma$ by a constant. Furthermore, with the self-similarity constraint the $\Delta\tau/b\sigma$ and $(1 - a/b)\ln(V_{max}/V_{bg})$ terms become the $g + (1 - a/b)$ that multiplies Ψ_0 in (A12). To the extent that (A12) is dominated by the Ψ_0-dependent term, $\ln(V\theta/D_c)$ could both have a minimum near the stress minimum and be near steady state at that point ($g_{min} \sim -[1 - a/b]$, so at $X = X_{gmin}$, $\ln[V\theta/D_c] \sim 0$) (Figure D1a).

[73] Estimating the extent to which the minima in $\ln(V\theta/D_c)$ and $\Delta\tau$ might differ requires evaluating the other terms in (A12). Taking the spatial derivative and writing Ψ for $\ln V\theta/D_c$ leads to

$$\frac{d\Psi}{dX} = g'\Psi_0 + \left(1 - \frac{a}{b}\right)\left[\frac{f''}{f'} + \frac{C}{V/(f'V_{max})}\right]. \tag{D1}$$

Closer to the tip than the stress minimum g' is large and negative, with a maximum magnitude of order unity (Figure D1b). In the vicinity of X_{gmin}, the f''/f' term, which accounts for the translation rather than the sharpening of the pulse front, dominates the bracketed expression because the denominator of the second term is of order 1 (see Figure 3, which also applies nearly unchanged to other a/b after scaling the horizontal axis by $[1 - a/b]^{-2}$). At X_{gmin}, $g' = 0$ and $f'' < 0$, so $d\Psi/dX < 0$ ($f'' < 0$ because the inflection point where $f'' = 0$ occurs very close to X_{Vm}, well inboard of X_{gmin}). Thus the minimum in Ψ, if it exists, occurs outboard of the minimum in $\Delta\tau$.

[74] Outside the slip-weakening region, g' is positive and close to $(1 - a/b)^3$ (equation (39)). For a crude estimate of f''/f' we can assume that outboard of X_{gmin} the slip satisfies the near-tip approximation, $\delta = (2\sqrt{2}/\sqrt{\pi}\mu')K_c\sqrt{x'}$, with K_c given by (7). This leads to $f(X) \approx (4/\sqrt{\pi})X^{-1/2}$, or

$$\frac{f''}{f'} \approx -\frac{1}{2X}. \tag{D2}$$

At $X = X_{gmin} \sim 7$, (D2) implies $f''/f' \sim -0.07$; numerically we find the value to be ~ -0.1 (Figure D1b). For $a/b = 0.9$ and $\Psi_0 > 10$ (that is, $V_{max}/V_{bg} > 10^4$), $(1 - a/b)^2\Psi_0 > 0.1$, so from (D1) we expect $d\Psi/dX$ to change from negative to positive before g' reaches the estimate of $(1 - a/b)^3$ from (39). From Figure D1a this occurs by $X = 9$; the actual minimum of Ψ occurs even closer to X_{gmin}.

[75] Qualitatively, we can say that $d\Delta\tau/dX$ passes from negative to positive because of the transition from the slip-weakening region to the dislocation-like stress field. Then dividing (D1) by $(1 - a/b)$ and with $g' = (1 - a/b)^3$, $d\Psi/dX$ will pass from negative to positive at near the same spot unless f''/f' is more negative than $(1 - a/b)^2\Psi_0$ is positive. If we assume $f = aX^n$, then $f''/f' = (n - 1)X^{-1}$. For a concave, crack-like slip profile, $0 < n < 1$. Within these bounds f''/f' can be at most twice that in (D2).

[76] **Acknowledgments.** This research was supported by NSF grant EAR-0538156. We thank an anonymous reviewer and the Associate Editor for detailed comments that helped clarify many aspects of the manuscript.

References

Ampuero, J.-P., and A. M. Rubin (2008), Earthquake nucleation on rate and state faults: Aging and slip laws, *J. Geophys. Res.*, *113*, B01302, doi:10.1029/2007JB005082.

Bayart, E., A. M. Rubin, and C. Marone (2006), Evolution of fault friction following large velocity jumps, *Eos Trans, AGU*, *87*(52), Fall Meet. Suppl., Abstract S31A-0180.

Beeler, N. M., T. E. Tullis, and J. D. Weeks (1994), The roles of time and displacement in the evolution effect in rock friction, *Geophys. Res. Lett.*, *21*, 1987–1990.

Blanpied, M. L., C. J. Marone, D. A. Lockner, J. D. Byerlee, and D. P. King (1998), Quantitative measure of the variation in fault rheology due to fluid-rock interactions, *J. Geophys. Res.*, *103*, 9691–9712.

Broberg, K. B. (1999), *Cracks and Fracture*, Academic, San Diego, Calif.

Chen, T., and N. Lapusta (2009), Scaling of small repeating earthquakes explained by interaction of seismic and aseismic slip in a rate and state fault model, *J. Geophys. Res.*, *113*, B01311, doi:10.1029/2008JB005749.

Dieterich, J. H. (1979), Modeling of rock friction: 1. Experimental results and constitutive equations, *J. Geophys. Res.*, *84*, 2161–2168.

Dieterich, J. H. (1992), Earthquake nucleation on faults with rate- and state-dependent friction, *Tectonophysics*, *211*, 115–134.

Dieterich, J. H. (1994), A constitutive law for rate of earthquake production and its application to earthquake clustering, *J. Geophys. Res.*, *99*, 2601–2618.

Dieterich, J. H., and B. D. Kilgore (1994), Direct observation of frictional contacts: New insights for state-dependent properties, *Pure Appl. Geophys.*, *143*, 283–302.

Dieterich, J. H., and B. D. Kilgore (1996), Implications of fault constitutive properties for earthquake prediction, *Proc. Natl. Acad. Sci. U. S. A.*, *93*, 3787–3794.

Ellsworth, E. L., and G. C. Beroza (1995), Seismic evidence for an earthquake nucleation phase, *Science*, *268*, 851–855.

Ellsworth, E. L., et al. (2007), Seismology inside the fault zone: Applications to fault-zone properties and rupture dynamics, *Sci. Drill.*, *Special Issue 1*, part 4, 84–87, doi:10.2204/iodp.sd.s01.04.2007.

Kaneko, Y., and N. Lapusta (2008), Variability of earthquake nucleation in continuum models of rate-and-state faults and implications for aftershock rates, *J. Geophys. Res.*, *113*, B12312, doi:10.1029/2007JB005154.

Kato, N. (2003), A possible model for large preseismic slip on a deeper extension of a seismic rupture plane, *Earth Planet. Sci. Lett.*, *216*, 17–25.

Kilgore, B. D., M. L. Blanpied, and J. H. Dieterich (1993), Velocity dependent friction of granite over a wide range of conditions, *Geophys. Res. Lett.*, *20*, 903–906.

Lawn, B. (1993), *Fracture of Brittle Solids*, 2nd ed., Cambridge Univ. Press, Cambridge, U. K.

Liu, Y., and J. R. Rice (2005), Aseismic slip transients emerge spontaneously in three-dimensional rate and state modeling of subduction earthquake sequences, *J. Geophys. Res.*, *110*, B08307, doi:10.1029/2004JB003424.

Marone, C. (1998), Laboratory-derived friction laws and their application to seismic faulting, *Annu. Rev. Earth Planet. Sci.*, *26*, 643–646.

Nakatani, M. (2001), Conceptual and physical clarification of rate and state friction: Frictional sliding as a thermally activated rheology, *J. Geophys. Res.*, *106*, 13,347–13,380.

Nakatani, M., and C. H. Scholz (2006), Intrinsic and apparent short-time limits for fault healing: Theory, observations, and implications for velocity-dependent friction, *J. Geophys. Res.*, *111*, B12208, doi:10.1029/2005JB004096.

Olson, E. L., and R. M. Allen (2005), The deterministic nature of earthquake rupture, *Nature*, *438*, 212–215, doi:10.1038/nature04214.

Perrin, G., J. R. Rice, and G. Zheng (1995), Self-healing slip pulse on a frictional surface, *J. Mech. Phys. Solids*, *43*, 1461–1495.

Reches, Z., M. Johnston, T. Jordan, T. Onstott, and M. Zoback (2004), Natural earthquake laboratory in South African mines: Drilling active faults and monitoring their seismicity, *Geophys. Res. Abstr.*, *6*, 06305.

Rice, J. R. (1993), Spatio-temporal complexity of slip on a fault, *J. Geophys. Res.*, *98*, 9885–9907.

Rice, J. R., N. Lapusta, and K. Ranjith (2001), Rate- and state-dependent friction and the stability of sliding between elastically deformable solids, *J. Mech. Phys. Solids*, *49*, 1865–1898.

Rubin, A. M. (2008), Episodic slow slip events and rate-and-state friction, *J. Geophys. Res.*, *113*, B11414, doi:10.1029/2008JB005642.

Rubin, A. M., and J.-P. Ampuero (2005), Earthquake nucleation on (aging) rate and state faults, *J. Geophys. Res.*, *110*, B11312, doi:10.1029/2005JB003686.

Ruina, A. (1983), Slip instability and state variable friction laws, *J. Geophys. Res.*, *88*, 10,359–10,370.

Secor, D., and D. Pollard (1975), On the stability of open hydraulic fractures in the Earth's crust, *Geophys. Res. Lett.*, *2*, 510–513.

Segall, P., and J. R. Rice (2006), Does shear heating of pore fluid contribute to earthquake nucleation?, *J. Geophys. Res.*, *111*, B09316, doi:10.1029/2005JB004129.

Shibazaki, B., and Y. Iio (2003), On the physical mechanism of silent slip events along the deeper part of the seismogenic zone, *Geophys. Res. Lett.*, *30*(9), 1489, doi:10.1029/2003GL017047.

J.-P. Ampuero, Seismological Laboratory, California Institute of Technology, Pasadena, CA 91125, USA.

A. M. Rubin, Department of Geosciences, Princeton University, Princeton, NJ 08544, USA. (arubin@princeton.edu)